Chapter 4: Catalytic Oxidation of NO on [Au-M]$^-$(M=Pd & Pt) Bimetallic Dimers: An Insight from DFT Approach

Abstract

In our previous chapter, we have reported catalytic oxidation of NO to NO_2 on $[Pt_2]^{0,\pm}$ dimers in which it was found that anionic Pt_2 system is the most efficient catalyst. However, it is important to improve the design of a suitable catalytic system that could perform the catalytic activity of the oxidation process more efficiently. Bimetallic dimers have gained attention because of their potential to alter their own properties by doping. Herein, in Chapter 4, a comprehensive theoretical investigation of the catalytic oxidation of NO on anionic bimetallic dimers [Au-M]$^-$(M=Pd, Pt) has been considered using Density Functional Theory (DFT) method using the same M06L/def2TZVP level of theory. Our adsorption energy calculations show that M-sites are found to be the preferred site for adsorption than Au-site. Further, full catalytic reaction pathways using Langmuir-Hinshelwood (L-H), Termolecular Eley-Rideal (TER) and Termolecular Langmuir-Hinshelwood (TLH) mechanism are investigated in which two NO molecules are converted to two NO_2 molecules in the presence of an activated O_2 molecule. On comparing the activation barriers for all the three mechanisms, it can be concluded that L-H mechanism is the favored pathway. Moreover, energetic span model has justified that conversion on [Au-Pd]$^-$ catalyst possesses a lower apparent activation energy than [Au-Pt]$^-$ which make [Au-Pd]$^-$ more efficient catalyst towards the catalytic conversion of NO into NO_2. Thus, the present study will convey us in understanding the mechanism of NO oxidation at the molecular level as well as designing better catalysts for future prospects.

Graphical Abstract

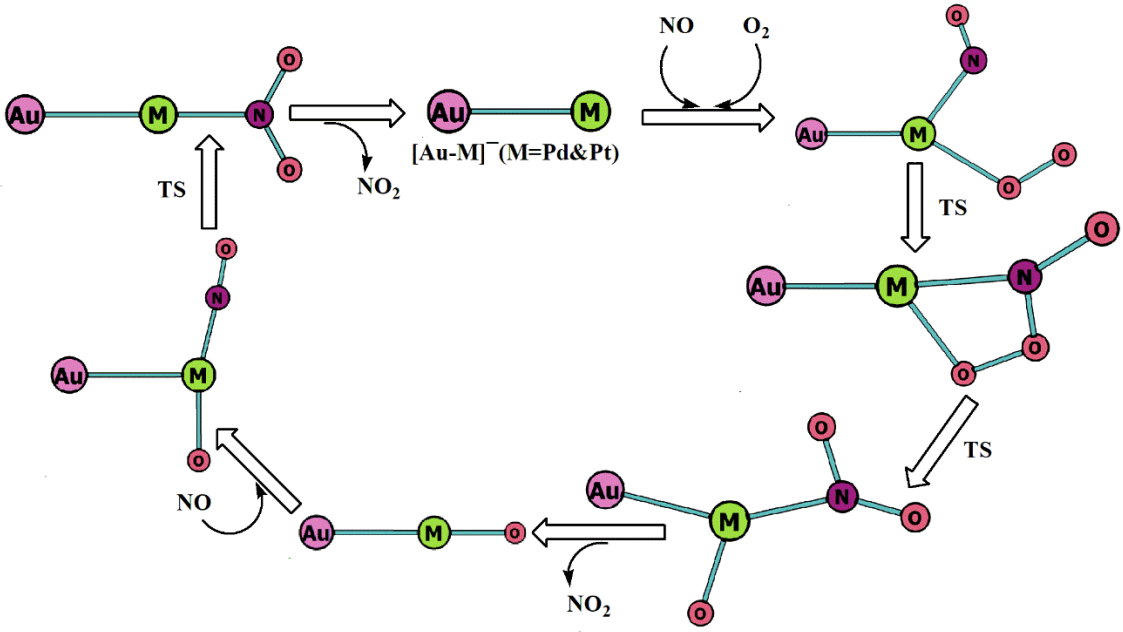

4.1. Introduction

Nitrogen Oxides (NO_x) abatement is one of the important steps for minimizing the harmful emissions which are released into the environment owing to the growth in the automobile industry. Automobiles are a significant source of carbon monoxide (CO) as well as NO_x. NO_x mainly includes Nitrogen monoxide (NO) and Nitrogen dioxide (NO_2) and the release of these gases causes environmental hazards such as photochemical smog and acid rain. Controlling NO_x emission has been made possible by introducing various methods such as three way catalysis (TWC), NO_x storage reduction (NSR), continuously regenerating trap (CRT) and selective catalytic reduction (SCR) [1-3]. In CRT, soot, a harmful byproduct of incomplete combustion, is collected on a diesel particulate filter. Therefore, NO is oxidised to NO_2, which in turn oxidizes soot [4]. It was found that the soot oxidation by NO_2 occurs at a much lower reaction temperature (greater than 300^0C) [5] than that of oxygen (500^0C-600^0C) [6, 7]. In a lean exhaust environment, SCR catalysts can control NO_x emission using an additional reductant. In NH_3-SCR process, it was found that reaction rate is greatly enhanced on retaining the equimolar feed of NO/NO_2 reaction mixture. When a fraction of NO is converted to NO_2 represented as $4NH_3+2NO+ 2NO_2 \rightarrow 4N_2+6H_2O$, the rate of reaction was found to be 10 times faster than standard SCR reaction ($4NH_3+ 4NO+O_2 \rightarrow 4N_2+6H_2O$) at a temperature range of 200 – 300 °C [8, 9]. In normal conditions, the NO oxidation efficiency is observed to be slow as a result of the complex nature of fuel gas and different particulate size distributions [10]. Thus, focus has to be on developing eligible catalyst for NO oxidation that could enhance NO conversion rate. It has been observed that nanoparticles of precious metals such as Au, Pd and Pt are extensively used in this regard due to their higher catalytic activity [4,11-14].

Consequently, considerable interest has been shown from both the industrial and scientific communities towards nano-sized gold clusters [15-18]. Gold nanoparticles exhibit catalytic activity on reactions such as low-temperature CO oxidation [19, 20], water gas shift reaction [21, 22] and direct propylene epoxidation using H_2 and O_2 [23, 24]. The catalytic activity of gold clusters can be tuned if alloying is done. Studies showed that when Au is mixed with metals such as Pd [25], Pt [26, 27] they show better catalytic activity corresponding to their

monometallic counterparts. As there is only 4% lattice mismatch between Au and Pd, they are completely miscible as a solid solution [28]. Wu and his co-workers found out that CO oxidation on AuPd (111) is easier compared to that of pure Pd (111) by density functional theory (DFT) calculations [29]. Au has the ability to electronically influence the catalytic property of Pd for the oxidation of alcohols [30]. An elaborative study was done on pseudomorphic monolayer Pt and Pd based alloys for NO oxidation [31]. Pt catalysts are also regarded as efficient catalysts for NO oxidation. Oxidation of NO on Pt catalysts has been studied thoroughly under different feed compositions [32-34]. Denton *et al.* [35] studied NO oxidation on Pt/SiO_2 and Pt/Al_2O_3 and found out that particle size of platinum plays a key role in controlling the activity. The basic approach to exploring the cluster properties is to understand it from an atom to a larger cluster size. Supported metal clusters are found to have excellent catalytic performance [36, 37], owing to its high specific surface area and distinctive electronic structure. Precious metals like Au, Pd and Pt are not only catalytically active but also expensive. So, decreasing the size of the clusters will also reduce the amount of active materials required. Recently, Graphene supported single metal atom and dimers are used as electrocatalyst for CO_2 reduction [38, 39]. Hence, getting the hindsight of the cluster's electronic properties and understanding the reaction at the molecular level becomes a necessary step for the modeling of realistic nanomaterials.

Numerous studies have been done on precious (Au, Pd, Pt, etc) monometallic as well as bimetallic metal clusters for NO oxidation [40-42]. But the mechanism of NO oxidation at the molecular level is still needed to be understood. In the present study, we propose for the first time NO oxidation using gas phase $[Au\text{-}M]^-$ (M=Pd, Pt) bimetallic dimers which proceeded via L-H, TER and TLH mechanisms. Anionic dimers are chosen for the catalytic NO oxidation because Au has the most electronegativity and the polarization effect is observed for the Au and its alloy nanoparticles, where it leads to the negatively charged systems. Therefore, anionic clusters are considered to be suitable for imitating the catalytic activities of Au and its alloying counterparts [43]. Gao *et al.* [44] also found that anionic gold clusters are better catalysts for CO oxidation than neutral ones as the negative charge on the anionic clusters improves the adsorption energy. Moreover, the energetic span

model [45] has also been used to find out the rate-determining states of the reaction pathway as well as the efficiency of the catalysts.

4.2. Computational Details

To obtain the lowest energy structures and thermo-chemical properties of the species involved in the reaction mechanism, Kohn-Sham density functional theory is used as implemented in Gaussian 09 software package [46] For geometry relaxation and frequency calculations, a local density M06L functional [47] is chosen which has a good result on both the main group and transition metals by establishing the dependency of the exchange-correlation energy on local spin density, spin density gradient, and spin kinetic energy density. Previous studies [48-52] also show the reliability of the M06L functional that it works quite well in producing the accurate structure and exploring the properties of precious metals. To locate the atomic orbitals of the atoms a density fitting triple zeta valence with single-polarization (def2TZVP) [53, 54] is employed in the calculation. Vibrational frequency calculations were done to distinguish between a minima {number of imaginary frequencies (NIMAG=0) and a first order maxima (NIMAG=1)}. IRC calculations [55, 56] have been performed to check the reliability of the reaction path. An ultrafine integration grid is taken into account for all the calculations.

Effect of mixing in binary alloys are determined by calculating the excess energy Δ which is given by-

$$\Delta = NE_{Au_m M_n} - mE_{Au_N} - nE_{M_N} \quad (1)$$

Where $E_{Au_m M_n}$ is the total zero-point corrected energy of the binary alloy and E_{Au_N} and E_{M_N} are the total zero-point corrected energies of the pure Au_N and M_N (M=Pd, Pt), respectively. Here N is equal to 2. Negative value of excess energy represents favorable mixing while positive value indicates demixing tendency.

The adsorption energy (E_{ads}) can be calculated as-

$$E_{ads} = E_{dimers/NO/O_2} - (E_{dimers} + E_{NO/O_2}) \quad (2)$$

where E_{dimers} represents the total zero-point corrected energy of the $[Au\text{-}M]^-$(M=Pd, Pt) bimetallic dimers, E_{NO/O_2} is the total zero-point corrected energy of the NO/O_2

molecule and E_{dimers/NO_2O_2} is the total zero point corrected energy of the NO/O_2 adsorbed on bimetallic dimers.

Natural Bond Orbital (NBO) [57] calculations have been performed with optimized geometries at M06L/def2TZVP level to provide insight into the reaction mechanism. Moreover, bond critical point has been calculated for the selected intermediates using AIMALL package [58].

We have implemented the energetic span model to calculate the energy span of the catalytic pathways that is developed by Shaik and Kozuch [45, 59, 60]. This model expresses the turn over frequency (TOF) as a function of energy span (δE) of the catalytic process. According to the model, in the catalytic cycle, rather having rate-determining step, it introduces rate-determining states that gives the apparent activation energy of the cycle. The transition state and intermediate that gives the apparent activation energy is introduced as turnover-frequency determining transition state (TDTS) and turnover-frequency determining intermediate (TDI).

$$TOF = \frac{K_B T}{h} e^{-\frac{\delta E}{RT}} \tag{3}$$

The TS that expands the δE more among all the transition states will be the TDTS and became the rate-determining transition state. The expression to calculate energy span (δE) is as follows,

$$\delta E = \begin{pmatrix} T_{TDTS} - I_{TDI}, \text{if TDTS appears after TDI} \\ T_{TDTS} - I_{TDI} + \Delta G_r, \text{if TDTS appears before TDI} \end{pmatrix} \tag{4}$$

Rate constant of each step in a catalytic oxidation reaction is obtained using well known kinetic theory, that is, Transition State Theory (TST) [61] and is usually expressed by the following relation:

$$k = \Gamma(T) \frac{k_B T}{h} e^{\left(\frac{-\Delta G^{TS}}{RT}\right)} \tag{5}$$

where Γ(T) represents the transmission coefficient, which is obtained from the following expression:

$$\Gamma(T) = 1 + \frac{1}{24}\left(\frac{h\nu^{\#}}{k_B T}\right)^2 \tag{6}$$

In Eq.(5), ΔG^{TS} is the difference of Gibbs free energy values for TS and reactants. In Eq. (6), $\nu^{\#}$ is the magnitude of the imaginary frequency of the transition state (TS). Other terms retain their normal meaning.

4.3. Results and Discussion

4.3.1 Electronic structures and properties of $[Au\text{-}M]^-$ (M=Pd, Pt) catalyst

Critical bond dissociation energies of Pt-O, Pt-N, Pd-O and Au-Pd bonds are calculated employing 15 different functionals along with density fitting triple-ξ def2TZVP basis set as shown in Table 4.1. Although B3PW91 has the least average deviation, M06L is found to perform relatively good in describing bond dissociation enthalpies of the bonds close to experimental data. To compare the results with the previous chapter, M06L functional is again chosen. Moreover, M06L is also found to be accurate in predicting the structures and properties of precious transition metals (as discussed in previous section).

Table 4.1: Benchmarking of 15 different functionals employing def2TZVP basis set with respect to experimental values of critical bond dissociation energy (BDE) of Pt-O, Pt-N, Pd-O and Au-Pd bond (in kJ/mol). (**PD**=Percentage Deviation; **APD**=Average Percentage Deviation)

Functionals	BDE (in kJ/mol)								
	Pt-O	PD	Pt-N	PD	Pd-O	PD	Au-Pd	PD	APD
B3LYP	375.78	10.09%	327.24	12.55 %	245.19	2.97%	152.02	6.53%	**8.03%**
B3P86	395.32	5.42%	346.61	7.37%	253.35	6.40%	159.77	11.96%	**7.78%**
B3PW91	377.87	9.59%	323.30	13.60 %	239.84	0.73%	151.80	6.37%	**7.57%**
HSEH1PBE	367.90	11.98%	313.11	16.32 %	231.45	2.79%	158.12	10.80%	**10.47%**
M06	354.42	15.21%	289.63	22.5%	192.95	18.96%	126.78	11.15%	**16.95%**
M06L	403.60	3.44%	343.17	8.29%	271.19	13.90%	166.30	16.54%	**10.54%**
M11L	353.42	15.45%	262.08	29.96 %	184.12	22.66%	107.53	24.64%	**23.17%**
M062x	294.16	29.62%	294.16	21.38 %	175.65	26.22%	84.53	40.75%	**29.49%**
mn12sx	383.66	8.21%	337.63	9.77%	210.97	11.39%	172.83	21.12%	**12.62%**

mpw1pw91	360.12	13.84%	303.43	18.91 %	223.79	6.01%	150.20	5.26%	**11.00%**
PBE	472.04	12.92%	431.61	15.34 %	332.48	39.64%	188.51	32.10%	**25.00%**
PBE0	370.26	11.42%	315.35	15.72 %	230.24	3.29%	154.18	8.04%	**9.61%**
TPSS	435.89	4.28%	392.60	4.91%	308.49	29.56%	192.65	35.01%	**18.44%**
TPSSh	397.59	4.88%	348.39	6.89%	268.54	12.78%	177.82	24.61%	**12.29%**
wb97xd	369.01	11.72%	305.11	18.46 %	213.66	10.26%	93.62	34.39%	**18.70%**
Exp.	**418 ±11.6 [62]**		**374 ±9.6 [62]**		**238.1 ±12.6 [62]**		**142.7 ±21 [62]**		

Figure 4.1 includes ground state electronic structures of $[Au\text{-}M]^-$ (M=Pd, Pt) dimers, NO and O_2 obtained at the M06L/def2TZVP level of theory. It also includes HOMO-LUMO isosurfaces along with their bond lengths (in Å) and NBO charges (shown in parentheses). As we have shown in Figure 4.1 that the bond lengths of $[Au\text{-}Pd]^-$ and $[Au\text{-}Pt]^-$ are 2.614 Å and 2.544 Å respectively. The ground state spin multiplicity of both the dimers is singlet. Our bond lengths are in good agreement with the previously reported bond lengths [63, 64]. The bond lengths of O_2, NO and NO_2 are found to be 1.205 Å, 1.147 Å, and 1.191 Å which are also very close to the values of bond lengths reported in CRC handbook of chemistry and physics [62]. The orientation of HOMO and LUMO of the catalysts and the reactants are depicted in Figure 4.1. It is noteworthy to discuss the HOMO and LUMO of the cluster as it provides information about the bonding nature of the cluster with the reactant molecules. HOMO and LUMO are similar in both the dimers. HOMO is concentrated on the 'd_{x2-y2}' orbital of Pd and Pt metal whereas the LUMO of the dimer located mainly on the s-d hybridized orbital of Pd and Pt. The contribution of orbitals to the HOMO and LUMO are shown in Table 4.2. Excess energy (Δ) is calculated for $[Au\text{-}Pd]^-$ dimer with respect to $[Au_2]^-$ and $[Pd_2]^-$ and Δ is calculated for $[Au\text{-}Pt]^-$ dimer with respect to $[Au_2]^-$ and $[Pt_2]^-$. The Δ is found to be negative (-11.92 kcl/mol) for $[Au\text{-}Pd]^-$ dimer which means mixing is favored in case of Au and Pd (for dimers). Whereas a positive value (5 kcal/mol) for $[Au\text{-}Pt]^-$ dimer indicates demixing tendency.

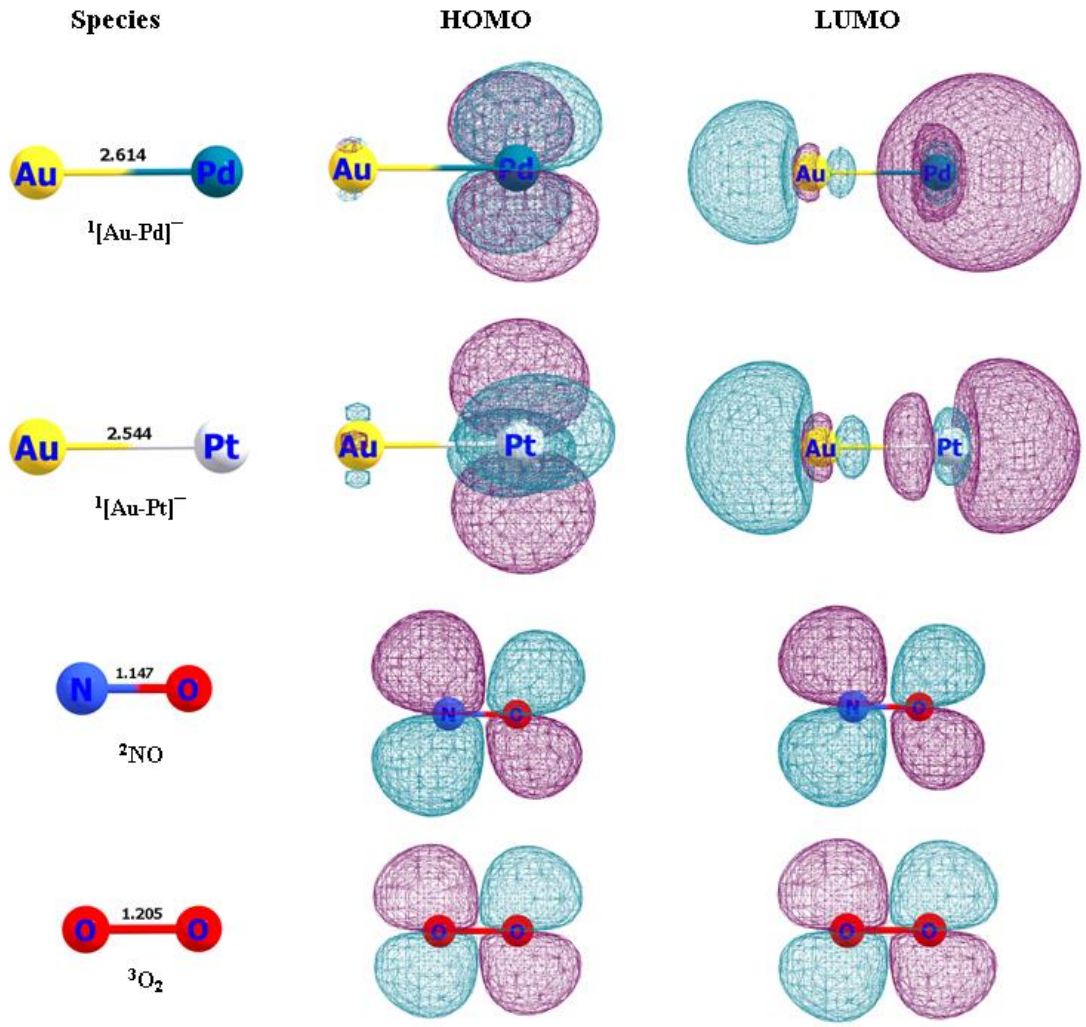

Figure 4.1: Optimized structures of [Au-M]$^-$ (M=Pd, Pt) dimers and the reactants (NO and O_2) along with their HOMO-LUMO isosurfaces obtained at the M06L/def2TZVP level of theory.

Figure 4.1 includes the NBO (or natural) charges of the initial geometries. It is found that the initial charges on [Au-Pd]$^-$ are -0.665e for Au, and -0.335e for Pd. This tells us that the electronic charge resides on Au site rather than Pd. In [Au-Pt]$^-$ dimer, electronic charge is more on Pt (-0.650e) rather than Au (-0.350e).

Table 4.2: Major contribution of orbitals to the HOMO and LUMO of [Au-M]$^-$ (M=Pd, Pt) dimer.

Species	Atom	Orbitals	Contribution
[AuPd]$^-$ HOMO	Pd	$4d_{x2-y2}$	99.54%

$[AuPd]^-$ LUMO	Au	6s	14.97%
	Pd	5s	70.17%
	Pd	$4d_z^2$	3.90%
$[AuPt]^-$ HOMO	Pt	$5d_{x2-y2}$	99.50%
$[AuPt]^-$ LUMO	Au	6s	27.59%
	Pt	6s	48.37%
	Pt	$5d_z^2$	13.55%

Talking about each cluster's electronic properties is crucial since it reveals important details on the catalysts' chemical reactivity. Table 4.3 lists the electronic properties of $[Au\text{-}M]^-$ (M=Pd, Pt) dimers including the HOMO-LUMO gap (HLG), chemical potential, hardness, softness, and electronegativity.

Table 4.3: Electronic properties of $[Au\text{-}M]^-$ (M=Pd, Pt) dimer, (HLG=HOMO-LUMO gap).

Catalyst	**Properties (in eV)**				
	HLG	**Hardness**	**Softness**	**Chemical Potential**	**Electro-negativity**
$[AuPd]^-$	0.890	0.445	1.122	1.807	-1.807
$[AuPt]^-$	0.301	0.150	3.313	1.456	-1.456

The HLG of $[Au\text{-}Pd]^-$ is 0.890 eV which is 0.59 eV higher than HLG of $[Au\text{-}Pt]^-$dimer. Moreover, other electronic properties such as hardness and softness reveals higher reactivity for $[Au\text{-}Pt]^-$dimer. $[Au\text{-}Pt]^-$ shows better chemical reactivity for the guest molecules than $[Au\text{-}Pd]^-$ and our adsorption energy values are in line with the conclusion given above.

4.3.2 Adsorption of NO/O_2 on $[Au\text{-}M]^-$(M=Pd, Pt) dimers, Adsorption Energy and Wiberg bond index

Adsorption of NO/O_2 on the catalytic sites is one of the most important steps as it determines the feasibility of the reaction. Thus we have first adsorbed NO/O_2 on $[Au\text{-}M]^-$(M=Pd, Pt) dimers using M06L/def2TZVP level of theory. Optimized geometries of NO/O_2 adsorbed dimers are shown in Figure 4.2 along with the bond parameters and NBO charges. Calculated single adsorption energies (E_{ads}) of NO/O_2 adsorbed on $[Au\text{-}M]^-$(M=Pd, Pt) dimers are listed in Table 4.4.

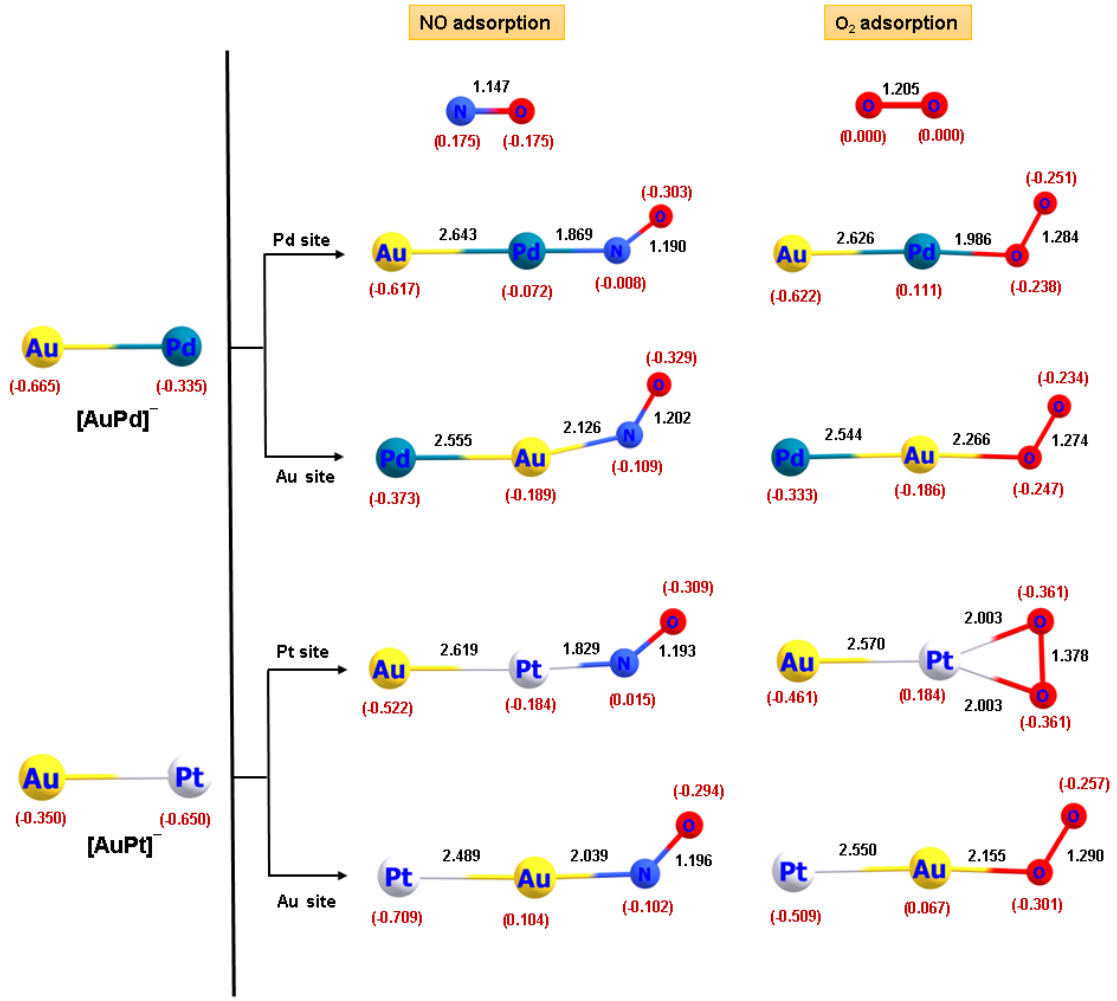

Figure 4.2: Optimized structures of NO/O_2 adsorbed dimers at M06L/def2TZVP level along with bond length (in Å) and NBO charges (in brackets).

Table 4.4: Calculated adsorption energy (in kcal/mol) of NO/O_2 adsorbed on the dimers [Au-M]$^-$ (M=Pd&Pt) at M06L/def2TZVP levels.

Adsorbed Species	[Au-Pd]$^-$ dimer		[Au-Pt]$^-$ dimer	
	Au site	Pd site	Au site	Pt site
NO adsorbed	-20.47	-53.75	-27.93	-66.65
O_2 adsorbed	-15.63	-38.83	-19.70	-40.55

It is clear from Table 4.4, that the value of adsorption energies for NO adsorbed on the Pd site of [Au-Pd]$^-$ and Pt site of [Au-Pt]$^-$ dimers is -53.75 kcal/mol and -66.65 kcal/mol, respectively at M06L/def2TZVP level, which is more than NO adsorbed on Au site of both the dimers. In the case of O_2 adsorbed on various sites of both dimers, the value of adsorption energies on Pd site of [Au-Pd]$^-$ and Pt site of [Au-Pt]$^-$ dimers are also having greater value than O_2 adsorbed on Au site of dimers. We further noticed that the value of adsorption energies of NO adsorbed on M-sites (i.e. Pd and Pt sites) is more negative than that of O_2 adsorbed on the same sites. It is to be noted that either atoms in NO is a potential donor, but nitrogen prefers to bind with the dimers so that a large formal negative large on a more electronegative oxygen atom could be avoided.

From adsorption energy calculations, it can be said that NO and O_2 prefer to bind with M site (M=Pd, Pt). However, on comparing the adsorption energy calculation, it was found that NO and O_2 have more affinity towards Pt. There has to be a reason to explain the stronger adsorption energies of NO and O_2 with Pt than that of Pd. It can be seen that as O_2 is adsorbed on Pd site of [Au-Pd]$^-$ dimer, an amount of 0.446e has been transferred from Pd to O_2 antibonding orbitals, leading to the weakening of O-O bond and strengthening of Pd-O bond. Similarly, if we compare the binding of O_2 with Pt site of [Au-Pt]$^-$ dimer, an electronic charge of 0.834e has been transferred from Pt to O_2 antibonding orbitals. This justifies the elongation of O-O bond length upto 1.378 Å when bonded with Pt site. In the case of NO adsorption, an amount of 0.263e and 0.466e has been transferred from Pd and Pt, respectively to NO. Therefore, differences in the adsorption energies of NO with Pd (-53.75 kcal/mol) and Pt (-66.65 kcal/mol) has been observed. Despite having a similar arrangement of HOMO and LUMO, we have observed a significant

difference in the binding energy pattern of NO and O_2 with the dimers. This effect is justified by the HOMO-LUMO energy gap (HLG) of both $[Au\text{-}Pd]^-$ and $[Au\text{-}Pt]^-$dimers.

Activation of O_2 is a crucial step in the oxidation of NO to NO_2. When O_2 is adsorbed on Pd site of $[Au\text{-}Pd]^-$ dimer, the O-O bond length is elongated to1.284 Å with respect to the free O_2 molecule (1.208 Å) which confirms the activation of O_2. The ground state spin multiplicity of $AuPd^-\text{-}O_2$ species is triplet. The vibrational frequency for the free O_2 molecule is 1633 cm^{-1}which reduces to 1238 cm^{-1} after binding with Pd-site of $[Au\text{-}Pd]^-$ dimer which indicates the strong donation of electron density from Pd atom to the antibonding orbital of O_2. On the other hand, when O_2 binds with the Au site of $[Au\text{-}Pd]^-$ dimer, its bond length is found to be 1.274 Å which is slightly less than that of the Pd–site. In Pt site of $[Au\text{-}Pt]^-$ dimer, O_2 binds by forming peroxide linkage and is termed as η2 ligation. The ground state spin multiplicity of $AuPt^-\text{-}O_2$ species is singlet. The elongation of O-O bond length on Pt site is 1.378 Å which is more than the Au site (1.290 Å). The vibrational frequency of O_2 before and after binding also supports the strength of the Pt-O bond (1633 cm^{-1} to 1045 cm^{-1}).

Moreover**,** Natural Bond Orbital (NBO) analysis is also carried out to obtain Wiberg bond index [65] that provides a comparative scale for the bond strength. In this regard, we have calculated the value of the Wiberg bond index for NO and O_2 adsorbed on $[Au\text{-}Pd]^-$ and $[Au\text{-}Pt]^-$ dimers (Table 4.5)

Table 4.5: Wiberg bond index for newly formed bonds after adsorption of NO and O_2 at M06L/def2TZVP level.

Adsorbed Species	**Wiberg bond index**			
	$[Au\text{-}Pd]^-$ dimer		**$[Au\text{-}Pt]^-$ dimer**	
	Au-N	Pd-N	Au-N	Pt-N
NO adsorbed	0.498	**0.919**	0.536	**1.126**
	Au-O	Pd-O	Au-O	Pt-O
O_2 adsorbed	0.234	**0.415**	0.422	**0.670**

For the adsorption of NO on the Pd site of $[Au\text{-}Pd]^-$ dimer, the value of the Wiberg bond index is 0.919 which is more than the adsorption of NO on Au site of the same dimer (bond index value of 0.498). We have observed the same trend in the case of NO adsorbed on $[Au\text{-}Pt]^-$ dimer where Pt site dominates the adsorption. In addition, the calculated Wiberg bond index for O_2 adsorbed products reveals the strong binding of O_2 on the M-site (M=Pd, Pt) of the catalysts compared to the Au-site.

4.3.3 Co-adsorption of NO and O_2, 2 NO and 2 O_2 on $[Au\text{-}M]^-$(M=Pd, Pt) dimers

Flue gas contains both NO and O_2, so it's critical to examine the different arrangements of the co-adsorption of O_2 and NO molecules, as well as two NO and two O_2 molecules. At the M06L/def2TZVP level of theory, Table 4.6 presents the co-adsorption energies (Co-E_{ads}) (in kcal/mol) on various sites of $[Au\text{-}M]^-$(M=Pd, Pt).

Table 4.6: Calculated Co-adsorption energies (Co-E_{ads}) (in kcal/mol) of NO and O_2, two NO and two O_2 molecules co-adsorbed on different sites of $[Au\text{-}M]^-$(M=Pd, Pt) dimers at M06L/def2TZVP level.

Catalyst	NO_O_2 (M site)		NO_O_2 (Au site)		NO_O_2 (Different sites)			
	SM	Co-E_{ads}	SM	Co-E_{ads}	SM	Co-E_{ads}	SM	Co-E_{ads}
$[AuPd]^-$	2	-71.92	4	-25.96	4	-51.79	2	-65.32
$[AuPt]^-$	2	-81.96	2	-35.88	2	-38.16	2	-76.57
	2 NO (M site)		2 NO (Au site)		2 NO (Different sites)			
	SM	Co-E_{ads}	SM	Co-E_{ads}	SM		Co-E_{ads}	
$[AuPd]^-$	3	-86.03	3	-32.72	3		-72.63	
$[AuPt]^-$	3	-96.13	1	-37.62	3		-81.01	
	2 O_2 (M site)		2 O_2 (Au site)		2 O_2 (Different sites)			
	SM	Co-E_{ads}	SM	Co-E_{ads}	SM		Co-E_{ads}	
$[AuPd]^-$	3	-57.99	3	-21.58	3		-38.35	
$[AuPt]^-$	3	-57.06	3	-24.13	3		-48.61	

From Table 4.6, it is evident that coadsorption of NO and O_2 is more preferred on M site of the $[Au\text{-}M]^-$(M=Pd, Pt) dimers than that of the Au site. Furthermore, the co-adsorption energy (Co-E_{ads}) favors the co-adsorption of two NO molecules in both the dimers, but the probability of two O_2 molecules co-adsorbing on dimers is minimal. Hence, co-adsorption properties of NO_O_2 and 2 NO are discussed in detail whereas co-adsorption properties of 2 O_2 is discarded. Various co-adsorption modes of NO_O_2 and 2 NO on anionic bimetallic dimers are shown in Figure 4.3 and Figure 4.4, respectively.

The Co-E_{ads} of NO and O_2 on Pd site (Structure I) of $[Au\text{-}Pd]^-$ dimer is -71.92 kcal/mol which is much higher than that of Au site (-25.96 kcal/mol; Structure II). Apart from configuration I and II, two more configurations, III_a and III_b (Figure 4.3) arises, when NO and O_2 are adsorbed on adjacent sites of $[Au\text{-}Pd]^-$ dimer. The Co-E_{ads} of III_a and III_b are -51.79 kcal/mol and -65.32 kcal/mol, respectively. Table 4.7 includes vibrational frequencies (in cm^{-1}) and Wiberg bond indices (WBI) for co-adsorption of NO and O_2 on $[Au\text{-}M]^-$ (M=Pd, Pt) dimers. From Table 4.7, it is evident that NO and O_2 are activated highest in structure III_a where NO is adsorbed on Au site and O_2 adsorbed on Pd site. The values of $\nu_{N\text{-}O}$ and $\nu_{O\text{-}O}$ for III_a are 1653.36 cm^{-1} and 1265.71 cm^{-1}, respectively, which indicates redshift in frequency. The subsequent WBI values for N-O and O-O are 1.762 and 1.266, respectively. For structure I, where the co-adsorption energy is found to be highest, the vibrational frequency values of υ_{N-O} and υ_{O-O} are found to be 1722.67 cm^{-1} and 1273.15 cm^{-1}, respectively and the subsequent WBI_{N-O} and WBI_{O-O}values are 1.875 and 1.296.

In a similar pattern to that of $[Au\text{-}Pd]^-$ dimer, there are 4 different configurations of NO and O_2 co-adsorbed on $[Au\text{-}Pt]^-$ dimer. The Co-E_{ads} of NO and O_2 on Pt site (Structure I/) of $[Au\text{-}Pd]^-$ dimer is higher (-81.96 kcal/mol) than that of the other configurations which means the probability of both the reactants adsorbing on Pt site is maximum. Whereas the prospect of co-adsorption of the reactants onto the Au site is minimum. Although the Co-E_{ads} is maximum for structure I/, Table 4.7 suggests that the activation of NO and O_2 is most in case of $III/_a$. The values of υ_{N-O} and υ_{O-O} for $III/_a$ are 1668.16 cm^{-1} and 1024.62 cm^{-1}, respectively, and its subsequent WBI values for N-O and O-O are 1.743 and 1.221, respectively.

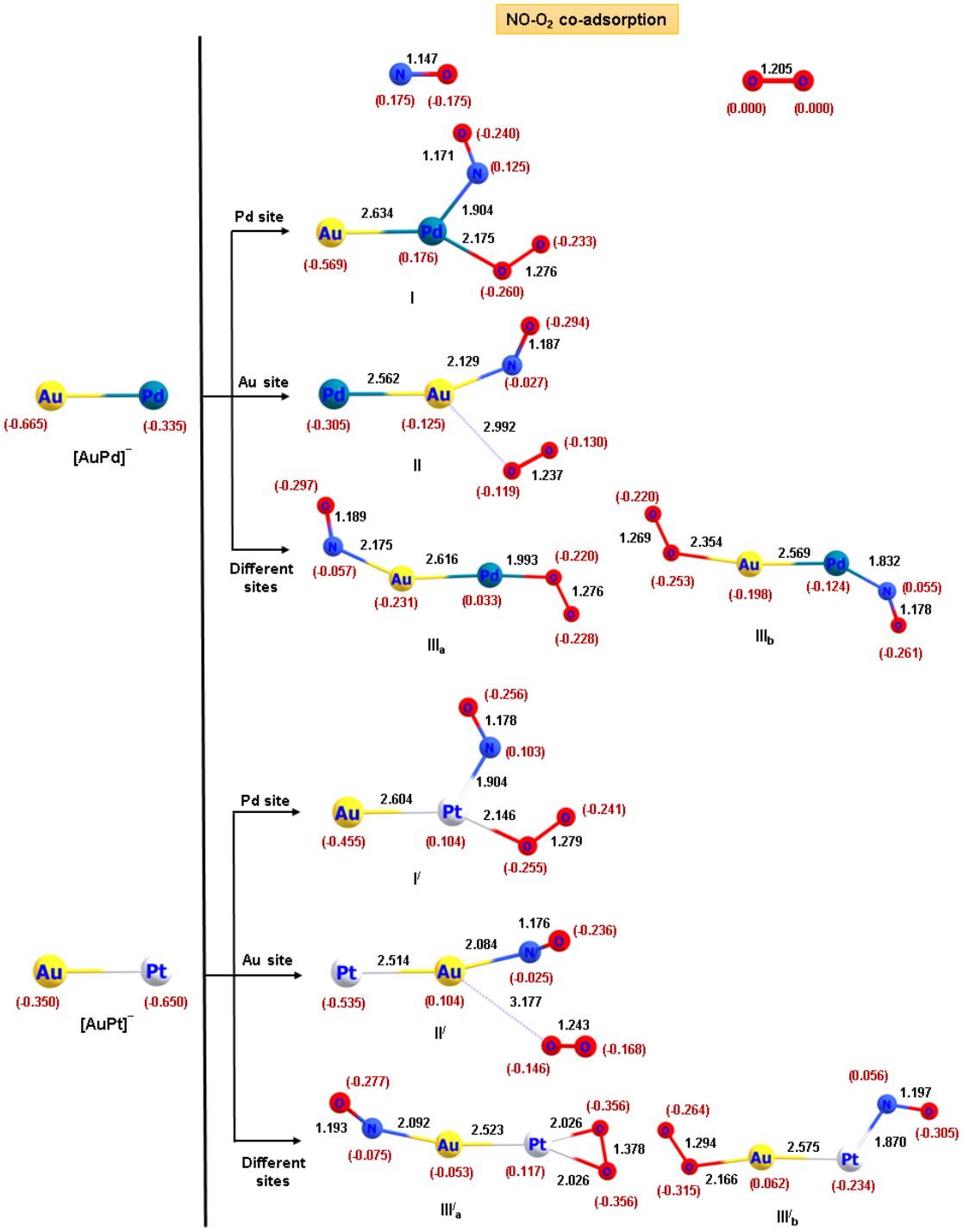

Figure 4.3: Optimized geometries of NO and O_2 co-adsorbed on $[Au\text{-}M]^-$ (M=Pd, Pt) dimers on different sites at M06L/def2TZVP level along with the bond parameters (in Å) and NBO charges (given in parentheses).

Table 4.7: Vibrational frequencies (in cm^{-1}) and Wiberg bond indexes (WBI) for co-adsorption of NO and O_2 on $[Au\text{-}M]^-$ (M=Pd, Pt) dimers.

Catalyst	I		II		III_a		III_b	
$[AuPd]^-$	υ_{N-O}	WBI_{N-O}	υ_{N-O}	WBI_{N-O}	υ_{N-O}	WBI_{N-O}	υ_{N-O}	WBI_{N-O}
	1722.67	1.875	1646.67	1.767	1653.36	1.762	1727.03	1.787
	υ_{O-O}	WBI_{O-O}	υ_{O-O}	WBI_{O-O}	υ_{O-O}	WBI_{O-O}	υ_{O-O}	WBI_{O-O}
	1273.15	1.296	1408.78	1.396	1265.71	1.266	1280.91	1.314
	I/		II/		$III/_a$		$III/_b$	
$[AuPt]^-$	υ_{N-O}	WBI_{N-O}	υ_{N-O}	WBI_{N-O}	υ_{N-O}	WBI_{N-O}	υ_{N-O}	WBI_{N-O}
	1683.69	1.842	1677.97	1.770	1668.16	1.743	1581.19	1.763
	υ_{O-O}	WBI_{O-O}	υ_{O-O}	WBI_{O-O}	υ_{O-O}	WBI_{O-O}	υ_{O-O}	WBI_{O-O}
	1255.84	1.284	1380.47	1.378	1024.62	1.221	1210.06	1.274

Structure IV depicts co-adsorption of 2 NO molecules on Pd site of $[Au\text{-}Pd]^-$ dimer whereas V depicts co-adsorption of 2 NO molecules on the Au site. Structure VI arises when 2 NO molecules are adsorbed adjacently on the anionic bimetallic dimer. The Co-E_{ads} of 2 NO on Pd site (Structure IV) is -86.03 kcal/mol which is higher than that of Structure V and VI. Hence, the probability of two NO molecules co-adsorbing on Pd site is more. Table 4.8 includes vibrational frequencies (in cm^{-1}) and Wiberg bond indices (WBI) for co-adsorption of 2 NO molecules on $[Au\text{-}M]^-$ (M=Pd, Pt) dimers. From Table 4.8, it can be seen that NO is more activated when it gets co-adsorbed on Au site of $[Au\text{-}Pd]^-$ dimer. The υ_{N-O} values for structure IV and V are 1673.11 cm^{-1} and 1619.05 cm^{-1}, respectively which means that NO is more activated when gets co-adsorbed on Au site rather than Pd site. It becomes more evident when 2 NO molecules are co-adsorbed adjacently. In structure VI, the υ_{N-O} values for Pd site and Au site are 1713.88 cm^{-1} and 1593.06 cm^{-1}, respectively which is indicating that NO adsorbed on Au site gets activated more in comparison to NO adsorbed on Pd site. It is attributed to the fact that electronic charge resides on Au more in case of$[Au\text{-}Pd]^-$ dimer. As a result, more charge is transferred from Au to

antibonding orbitals of NO. The WBI values of N-O on Pd (1.736) and Au site (1.668) of structure VI also depiciting greater elongation (or activation) of NO on Au site.

Structure IV/ and V/ depicts co-adsorption of 2 NO molecules on Pt site and Au site of $[Au\text{-}Pt]^-$ dimer, respectively whereas structure VI/ is formed when 2 NO molecules are adsorbed adjacently on of $[Au\text{-}Pt]^-$ dimer. Similar to $[Au\text{-}Pd]^-$ dimer, the Co-E_{ads} of 2 NO on Pt site (Structure IV/) is higher (-96.13 kcal/mol) than that of V/ and VI/ which means that co-adsorption of 2 NO molecules are preferable on Pt site of bimetallic dimer. In structure VI/, it can be seen that on co-adsorbing adjacently, NO molecule is more activated on Pt site (υ_{N-O} = 1521.64 cm^{-1} than that of Au site (υ_{N-O} = 1586.64 cm^{-1}). It is due to the fact that electronic charge resides on Pt site of $[Au\text{-}Pt]^-$ dimer. Hence, more charge is transferred from Pt d-orbitals to antibonding π* orbitals of NO.

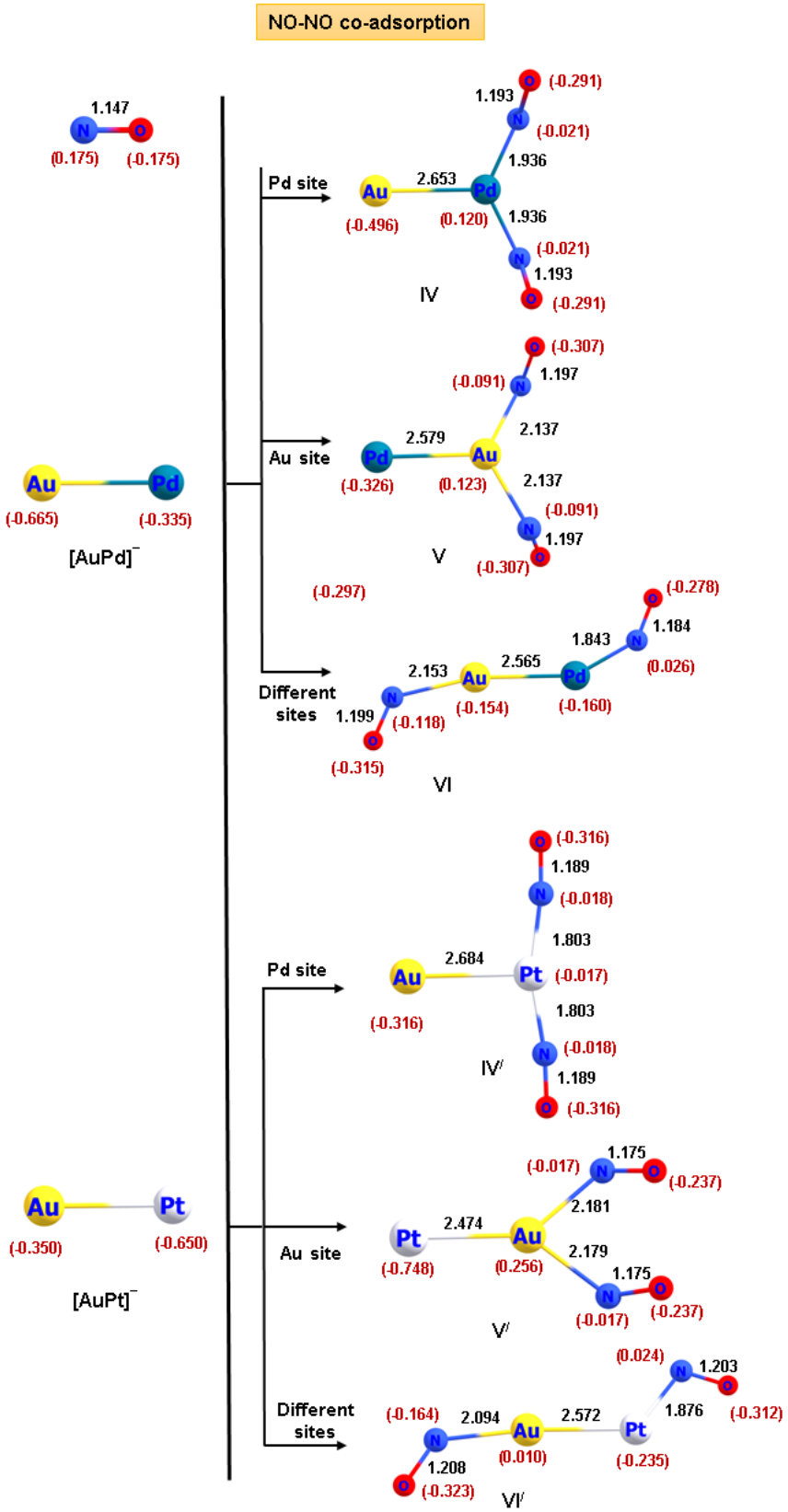

Figure 4.4: Optimized geometries of 2 NO co-adsorbed on [Au-M]⁻ (M=Pd, Pt) dimers on different sites at M06L/def2TZVP level along with the bond parameters (in Å) and NBO charges (given in parentheses).

Table 4.8: Vibrational frequencies (in cm^{-1}) and Wiberg bond indexes (WBI) for co-adsorption of 2 NO molecules on $[Au\text{-}M]^-$ (M=Pd, Pt) dimers.

Catalyst	IV		V		VI	
$[AuPd]^-$	υ_{N-O}	$WBI_{N\text{-}O}$	υ_{N-O}	$WBI_{N\text{-}O}$	υ_{N-O} (Pd)	$WBI_{N\text{-}O}$(Pd)
	1673.11	1.693	1619.05	1.691	1713.88	1.736
	υ_{N-O}	$WBI_{N\text{-}O}$	υ_{N-O}	$WBI_{N\text{-}O}$	υ_{N-O} (Au)	$WBI_{N\text{-}O}$(Au)
	---	---	---	---	1593.06	1.668
	IV/		V/		VI/	
$[AuPt]^-$	υ_{N-O}	$WBI_{N\text{-}O}$	υ_{N-O}	$WBI_{N\text{-}O}$	υ_{N-O} (Pt)	$WBI_{N\text{-}O}$(Pt)
	1764.99	1.653	1745.32	1.863	1521.64	1.709
	υ_{N-O}	$WBI_{N\text{-}O}$	υ_{N-O}	$WBI_{N\text{-}O}$	υ_{N-O} (Au)	$WBI_{N\text{-}O}$(Au)
	---	---	---	---	1586.64	1.614

4.3.4 Catalytic oxidation pathway of NO on $[Au\text{-}M]^-$(M=Pd, Pt) dimer

4.3.4.1 Langmuir Hinshelwood (L-H) mechanism

Strong adsorption on the catalyst tends to activate the adsorbates positively. From the above discussion, it was found that both NO and O_2 get adsorbed strongly on the M site of the dimers. Therefore, both the adsorbates are on the same site of the catalyst with high adsorption energies. This facilitates the interaction among the adsorbates and the reaction to proceed further. So, L-H mechanism [66, 67] has been considered in the present study to map out the full minimum energy reaction pathway. The proposed mechanism is likely to be followed as:

$$[Au\text{-}M]^- + NO\ (gas) + O_2\ (gas) \rightarrow [Au\text{-}M]^-O_2NO\ (coads)$$

$$[Au\text{-}M]^-O_2NO\ (coads) \rightarrow [Au\text{-}M]^-O\ (ads) + NO_2(gas)$$

$$[Au\text{-}M]^-O\ (ads) + NO\ (ads) \rightarrow [Au\text{-}M]^-\ ONO\ (coads)$$

$$[Au\text{-}M]^-\ ONO\ (coads) \rightarrow [Au\text{-}M]^- + NO_2\ (gas)$$

Overall reaction: $[Au\text{-}Pd]^- + 2NO\ (gas) + O_2\ (gas) \rightarrow [Au\text{-}Pd]^- + 2NO_2\ (gas)$

Optimized geometries of intermediates and transition states for NO oxidation on $[Au\text{-}Pd]^-$ along with bond length (in Å) are shown in Figure 4.5.

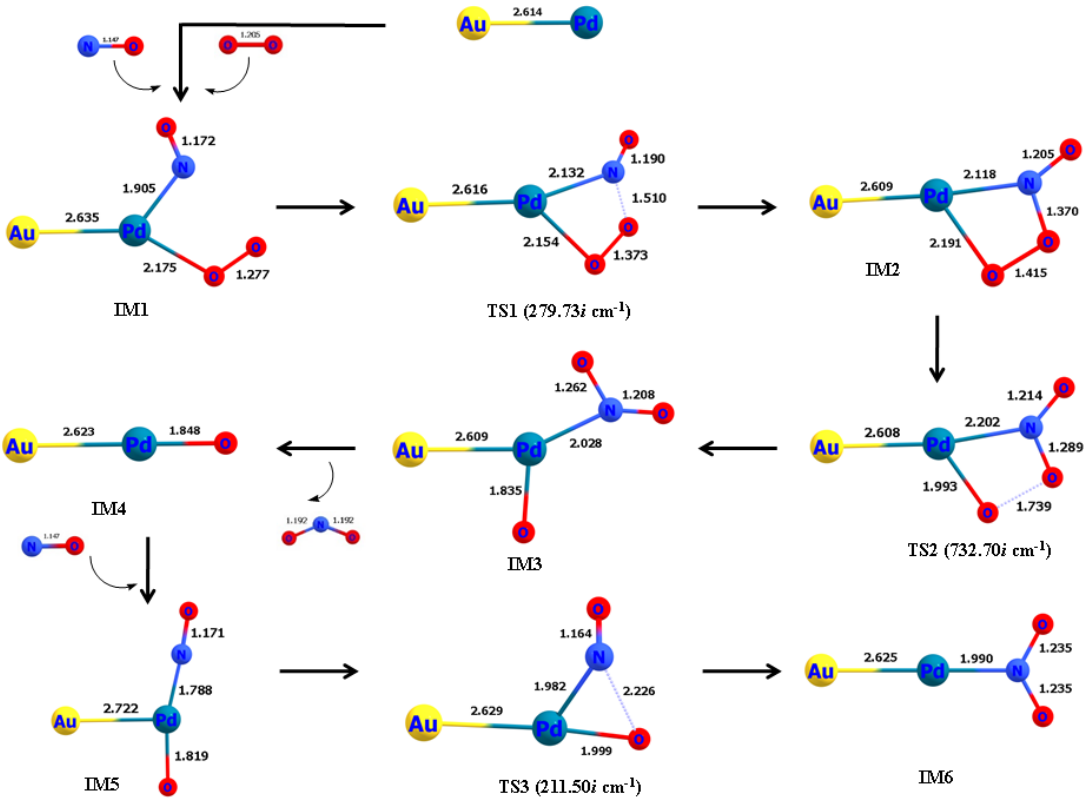

Figure 4.5: Optimized geometries of intermediates and transition states for catalytic oxidation of NO on $[Au\text{-}Pd]^-$dimer at M06L/def2TZVP level.

The reaction mechanism starts with the co-adsorption of NO and O_2 on the Pd site of the $[Au\text{-}Pd]^-$ dimer to form an intermediate (IM1). In the co-adsorbed intermediate IM1, the NO and O_2 bond lengths are observed 1.172 Å and 1.277 Å while Pd-N and Pd-O bond lengths are found to be 1.905 Å and 2.175 Å respectively. Further, IM1 proceeds through a transition state TS1 in which the unbound O interacts with the 'N' of NO to form IM2 (Figure 4.5). In the TS1, the O-O bond length elongates from1.277 Å to 1.373 Å which indicates that the O_2 has activated and ready to interact with the co-adsorbed NO. In the IM2, the bond distance of newly formed N-O decreases from 1.510 Å to 1.370 Å. Further, IM2 passes through a transition state TS2 where O-O bond cleavage takes place which results in the formation of NO_2 along with the IM3. Finally, in IM3, one NO_2 is formed and is subsequently removed, forming IM4. After this step, one NO molecule enters the system from the gas phase and gets co-adsorbed on the Pd-site of $[Au\text{-}Pd]^-O$ species and we have termed it as IM5. In the last step, the co-adsorbed NO interacts with

the remaining 'O' on the catalyst and forms another $NO_2$where this transition is reflected in TS3. After forming NO_2, it remains with the catalyst as IM6.

In this part, we have followed the catalytic oxidation pathway of NO on [Au-Pt]$^-$dimer which has the same mechanism as discussed in [Au-Pd]$^-$dimer. In this case, only Pd metal is replaced by Pt metal. In order to understand the reaction mechanism, optimized geometry of intermediates and transition states of [Au-Pt]$^-$dimer is shown in Figure 4.6 along with bond lengths (in Å).

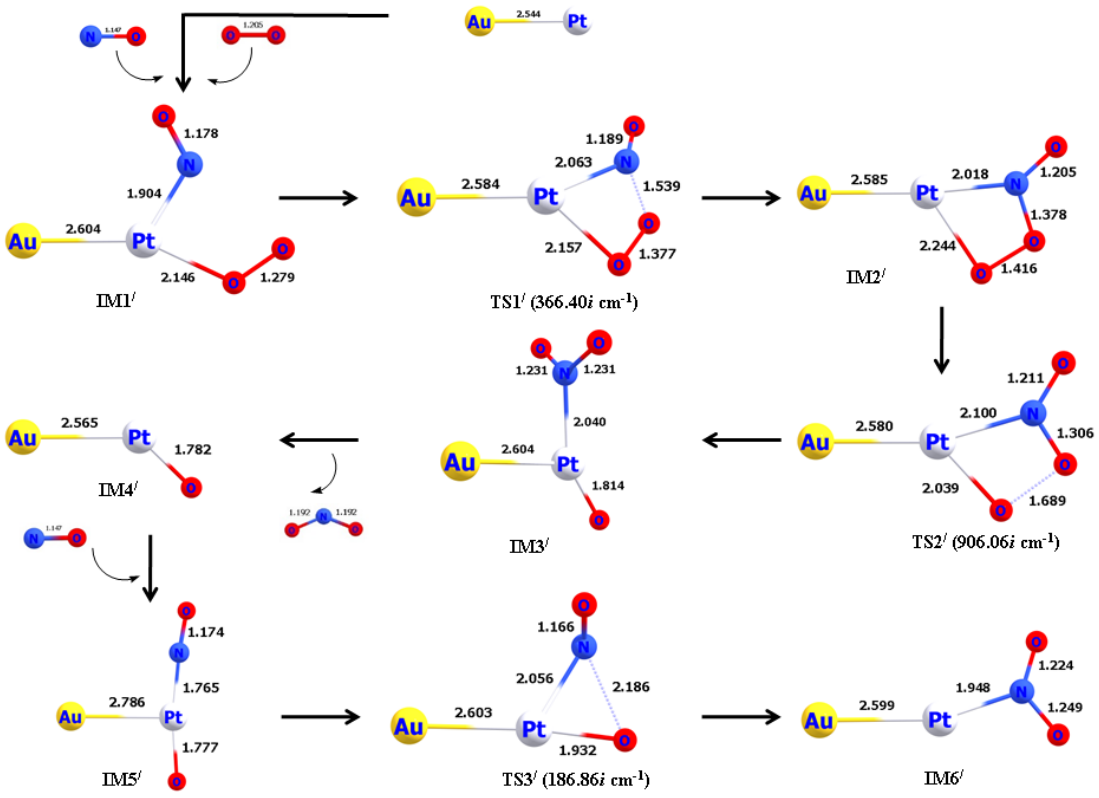

Figure 4.6: Optimized geometries of intermediates and transition states for catalytic oxidation of NO on [Au-Pt]$^-$dimer at M06L/def2TZVP level.

Like the previous catalyst, [Au-Pt]$^-$also shows a similar trend. IM1/ is formed by co-adsorption of O_2 and NO on the Pt site of the catalyst. The IM1/is much lower in energy than the starting material (-64.86 kcal/mol). The interaction of one of the O-atom occurs with NO resulting in the formation of TS1/ (366.40***i*** cm^{-1}). The barrier height of the TS1/ is 25.38 kcal/mol. IM2/ is formed with the weakening of the O-O bond length (1.377 Å to 1.416 Å) and consolidation of the N-O bond (1.539 Å to 1.378 Å). Finally, O-O bond breaks in TS2/ having imaginary frequency 906.06***i*** cm^{-1}. This step is facilitated by a lower barrier height, i.e. 7.97 kcal/mol. IM3/ is

formed in which one NO_2 is formed. The step is followed by the removal of one NO_2 molecule, forming IM4/. The NO molecule is co-adsorbed with [Au-Pt]$^-$O species (IM4/) forming IM5/. In the third transition state (TS3/), the single O atom gets closer to the lone NO molecule which on going further, forms the second NO_2 molecule in IM6/. However, the barrier height of the second NO_2 formation is very high (42.96 kcal/mol). The step is characterized by an imaginary frequency of 186.86***i*** cm^{-1}. All the TSs are authenticated using IRC calculations. It is to note that the spin is conserved throughout the reaction pathway.

We have obtained the value of the Gibbs' free energies of all the species as given in the reaction mechanism along with intermediates and transition states and plotted the energy profile diagram for the reaction as proposed in the above and shown in Figure 4.7.

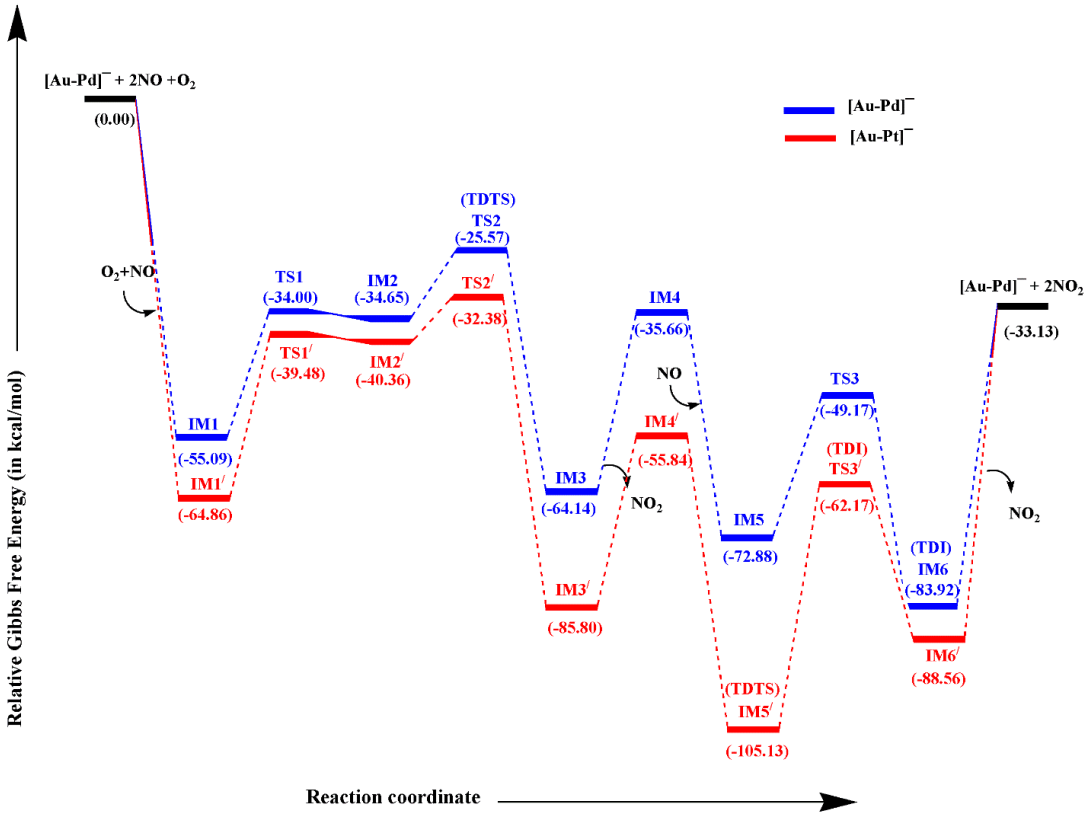

Figure 4.7: Potential energy diagram for catalytic oxidation pathway of NO on [Au-M]$^-$ (M=Pd, Pt) dimer at M06L/def2TZVP level. The rate-determining states have been labeled.

We have calculated relative Gibbs' free energies for all species with respect to [Au-M]$^-$ + 2NO (gas) + O_2 (gas) at 298 K and 1 atm. It is to be noted that when the reactant species (NO and O_2) gets adsorbed to the dimers, energy is released due to

the formation of new bonds. Therefore, all the intermediates are lower in energy as compared to total energy of the dimer and the reactant species. It is obvious from Figure 4.7 that NO and O_2 gets coadsorbed on the dimer and forms IM1 and IM1/ which has energy equal to -55.09 kcal/mol and -64.86 kcal/mol, respectively, lower than the starting species. The energy barrier of TS1 is 21.08 kcal/mol with respect to IM1 and TS1 is characterized by the presence of an imaginary frequency of 279.73***i*** cm^{-1}. We further obtained an intermediate IM2 which is lower energy than TS1. The energy barrier of TS1/ is 25.38 kcal/mol with respect to IM1/. Further, IM2 passes through a transition state TS2 where O-O bond cleavage takes place which results in the formation of NO_2 along with the IM3. The energy barrier of TS2 is found to be 9.08 kcal/mol with an imaginary frequency of 732.70***i*** cm^{-1}. The energy barrier of TS2/ is found to be 7.97 kcal/mol with an imaginary frequency of 906.06*i* cm^{-1}. After IM3 (and IM3/), one NO_2 is removed, thus forming $[Au\text{-}M]^-O$ species which is termed as IM4 and IM4/. After IM4, one NO molecule enters the system from the gas phase. The new structure IM5 and IM5/ in the PES (Figure 4.7) are 37.22 kcal/mol and 49.29 kcal/mol lower in energy than IM4 and IM4/, respectively. The last TS (TS3) is characterized by an imaginary frequency of 211.50***i*** cm^{-1} where the formation of the second NO_2 takes place. For TS3/, the imaginary frequency has a value of 186.86*i* cm^{-1}. In the PES diagram (Figure 4.7), after the formation of IM6, we have extended the graph to the free energy formation of NO_2 that is obtained from the free energy diffrerence between reactant and product.

Table 4.9: Calculated barrier heights (in kcal/mol) for both the anionic dimers via LH mechanism at M06L/def2TZVP level.

$[Au\text{-}Pd]^-$		**$[Au\text{-}Pt]^-$**	
Transition States	**Barrier Height**	**Transition States**	**Barrier Height**
TS1	21.08	TS1/	25.38
TS2	9.08	TS2/	7.97
TS3	23.70	TS3/	42.96

The activation energies for the process of NO oxidation on both the dimers have been shown in Table 4.9. For $[Au\text{-}Pt]^-$ catalyst, the barrier height of TS1/ is 25.38 kcal/mol, which is 4.30 kcal/mol more than TS1. TS2/ has a lower barrier height of 7.97 kcal/mol in comparison to TS2.

However, major difference is observed in the TS for the generation of second NO_2 molecule i.e. TS3 and TS3/. This fact can be described from the stability of IM5 and IM5/ in the reaction pathway. As we can see, that the IM5/ is much more stable in the PES (Figure 4.7) than IM5. This is a consequence of the binding nature of the catalyst with the second NO in the reaction pathway. To understand this, we have calculated the adsorption energies of NO on IM4 (and IM4/) for the formation of IM5 (and IM5/). We found out that the adsorption energy values for the adsorption of NO on IM4 and IM4/ are -43.33 kcal/mol and -54.65 kcal/mol, respectively. Adsorption energy values reveals that NO binds strongly with IM4/ than that of the IM4, thus making a more stable intermediate IM5/. This is the effect of the strong binding nature of NO with Pt site in the dimer for which IM5/ possesses high orbital reorganization energy which makes it difficult to reach IM6/. After the formation of second NO_2 (IM6 & IM6/), we have observed that NO_2 does not leave the catalytic sites and it maintain a bond distance of 1.990 Å and 1.948 Å with Pd (IM6) and Pt (IM6/) respectively. The desorption energies for the release of first and second NO_2 from $[Au\text{-}Pd]^-$ dimer are 28.47 kcal/mol and 50.79 kcal/mol, respectively. Similarly, first and second NO_2 are released from the $[Au\text{-}Pt]^-$ dimer at desorption energies of 29.95 kcal/mol and 55.43 kcal/mol, respectively. From the PES, it is seen that desorption energy for NO_2 to leave the catalytic site is higher in Pt than that of Pd. In the structure of NO_2 nitrogen possesses a single non-bonded electron on the 'N' atom which is responsible for the formation of Pd-N and Pt-N in the IM6 and IM6/ respectively. It can be described form the bond critical point of the IM6 and IM6/. The ESP value for the Pd-N is 0.13e lower than that of Pt-N which indicates that a relatively higher energy is required to break Pt-N bond in IM6/ than Pd-N in IM6.

4.3.4.2 Termolecular Eley Rideal (TER) mechanism

The TER mechanism is a three-molecular reaction that activates the gaseous O_2 molecule using two pre-adsorbed NO molecules. As previously discussed, the co-adsorption of two NO molecules on $[Au\text{-}M]^-$ (M=Pd, Pt) dimers is stronger than the

co-adsorption of NO and O_2 or the single adsorption of NO and O_2. Hence, NO oxidation is highly likely to proceed via TER mechanism. Moreover, TER mechanism has been considered in previous studies [68, 69] for catalytic oxidation of NO. The initial co-adsorption of two NO molecules is taking place at M site of the $[Au\text{-}M]^-$ dimer. The proposed mechanism for TER is likely to be followed as (* means attached to the catalyst):

$[Au\text{-}M]^- + 2\ NO\ (gas) + O_2\ (gas) \rightarrow [Au\text{-}M]^-ON^*N^*O\ (coads) + O_2\ (gas)$

$[Au\text{-}M]^-ON^*N^*O\ (coads) + O_2\ (gas) \rightarrow [Au\text{-}M]^-ON^*OON^*O\ (coads)$

$[Au\text{-}M]^-ON^*OON^*O\ (coads) \rightarrow [Au\text{-}M]^-\ O_2N^*N^*O_2\ (coads)$

$[Au\text{-}M]^-\ O_2N^*N^*O_2\ (coads) \rightarrow [Au\text{-}M]^- + 2\ NO_2\ (gas)$

Figure 4.8 and Figure 4.9 demonstrate, respectively, the optimized geometries of intermediates and transition states involved in the catalytic oxidation pathway of NO on $[Au\text{-}Pd]^-$ and $[AuPt]^-$ via TER mechanism.

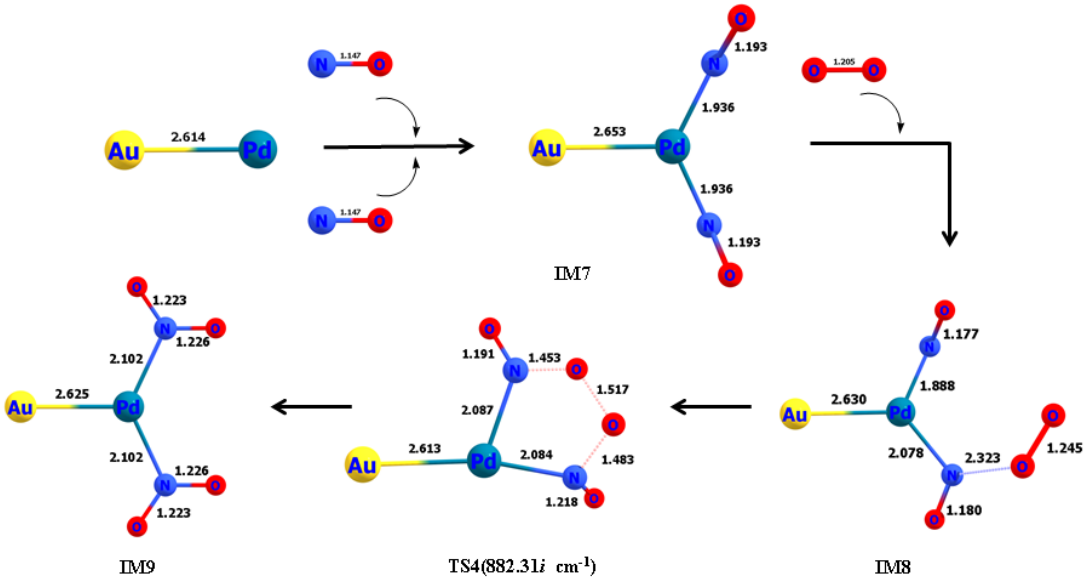

Figure 4.8: Optimized geometries of intermediates and transition states involved in catalytic oxidation pathway of NO on $[Au\text{-}Pd]^-$ dimer via TER mechanism along with their bond lengths (in Å).

The reaction begins with the co-adsorption of two NO molecules on the Pd site of the $[Au\text{-}Pd]^-$ dimer, resulting in IM7. This intermediate has a higher energy stability (69.04 kcal/mol) than the starting material. Inclusion of an O_2 molecule results in the production of IM8, which has slightly higher energy (10.72 kcal/mol) than IM7. The bond distance in IM8 shows that O_2 has a weak connection with one

NO molecule (2.323 Å) and barely any interaction with the Pd atom. The O-O bond length and υ_{O-O} in IM8 are 1.245 Å and 1371.04 cm^{-1}, respectively, indicating modest activation of O_2. The reaction proceeds through TS4, where O_2 reacts with two NO molecules adsorbed on the Pd atom of the anionic dimer. This TS is confirmed by its imaginary frequency 882.31***i*** cm^{-1} and the barrier height for this step is 33.93 kcal/mol. Hence, kinetically, the reaction mechanism is not too favourable at the room temperature as the transition barrier is somewhat high. The final intermediate is IM9 where two NO_2 molecules are fully formed and attached to the dimer catalyst. The desorption energy for two NO_2 molecules from $[Au\text{-}Pd]^-$ catalyst is 66.04 kcal/mol which is attainable at room temperature [70].

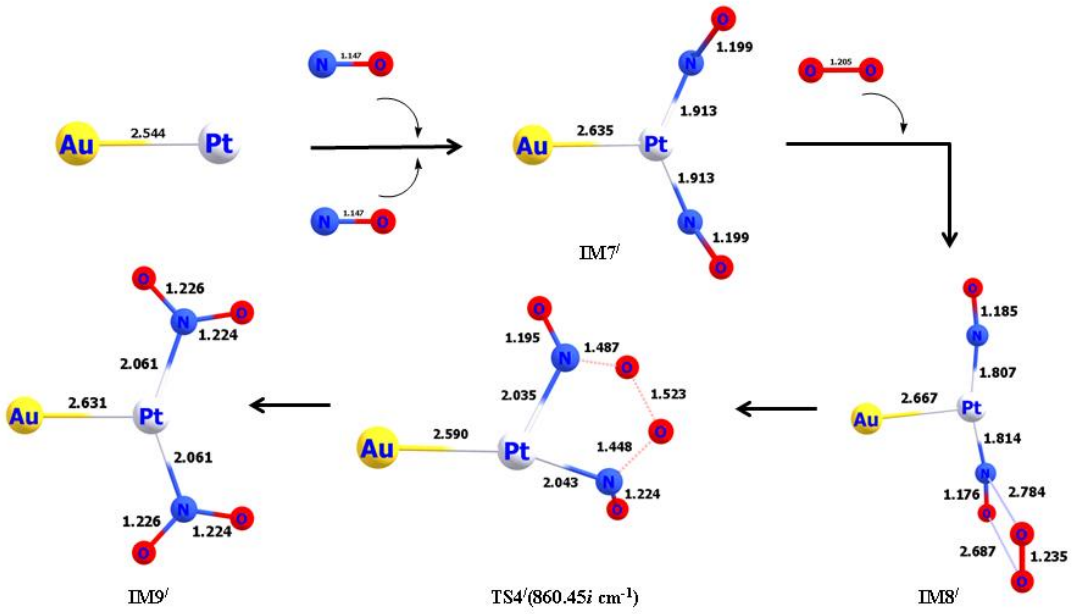

Figure 4.9: Optimized geometries of intermediates and transition states involved in catalytic oxidation pathway of NO on $[Au\text{-}Pt]^-$ dimer via TER mechanism along with their bond lengths (in Å).

Adsorption of two NO molecules on $[Au\text{-}Pt]^-$ dimer results in the formation of IM7/, which has a lower energy than the starting point (78.88 kcal/mol). The addition of O_2 to IM7/ produces IM8/, which has a lower energy than IM7/ (by 6.97 kcal/mol). O_2 interacts with a NO molecule from a distance (2.687 Å and 2.784 Å), remaining in the gas phase. The bond length (1.235 Å) and frequency (1422.98 cm^{-1}) indicate minimal O_2 activation in IM8/. The reaction proceeds via TS4/ (860.45***i*** cm^{-1}), where the O-O bond breaks while interacting with two NO molecules. In TS4/, the O-O bond elongates (1.523 Å) and two additional N-O bonds (1.487 Å and 1.448

Å) are formed. The activation barrier going from IM8/ to TS4/ is 54.85 kcal/mol. At last, IM9/ is formed where two NO_2 molecules are formed which is very much stable in PES (-104.87 kcal/mol). Two NO_2 molecules from the $[Au\text{-}Pt]^-$ catalyst have a desorption energy of 71.75 kcal/mol. Whole TER mechanism proceeds in triplet spin state (SM=3) for both the $[Au\text{-}M]^-$ dimer. The energy profile diagram for the TER reaction mechanism is shown in Figure 4.10.

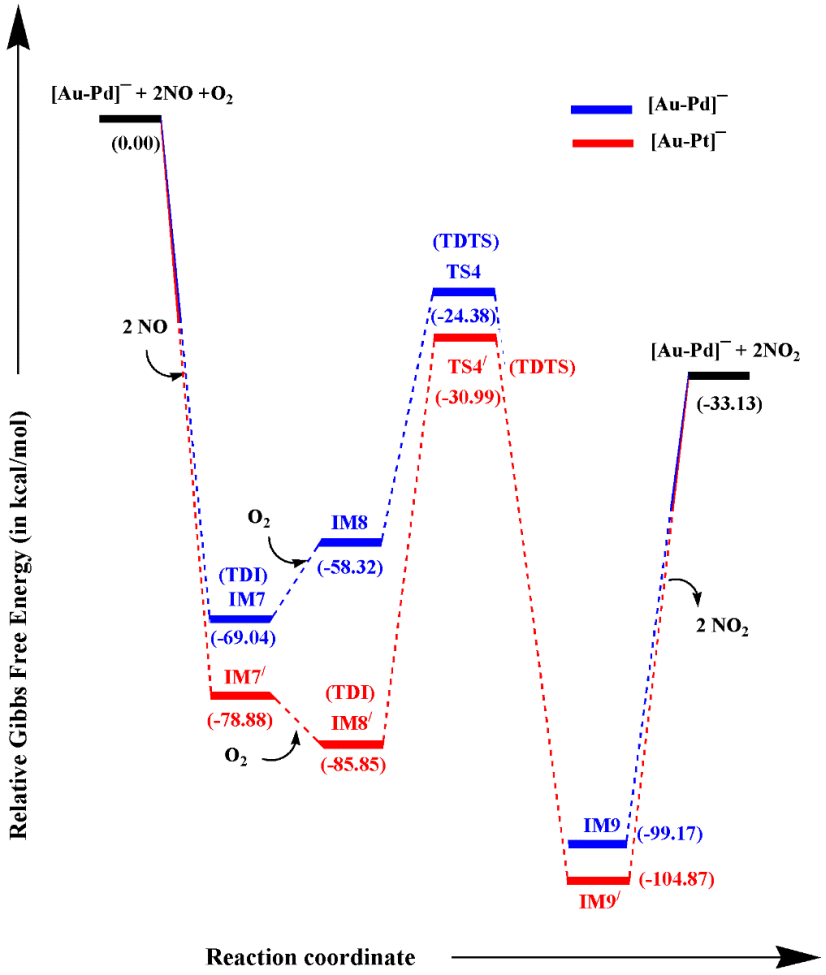

Figure 4.10: Potential energy diagram for catalytic oxidation pathway of NO on $[Au\text{-}M]^-$ (M=Pd, Pt) dimer via TER mechanism at M06L/def2TZVP level. The rate-determining states have been labeled.

Table 4.10 contains calculated barrier heights (in kcal/mol) for both the anionic dimers via TER mechanism at M06L/def2TZVP level.

Table 4.10: Calculated barrier heights (in kcal/mol) for both the anionic dimers via TER mechanism at M06L/def2TZVP level.

$[Au\text{-}Pd]^-$		$[Au\text{-}Pt]^-$	
Transition States	**Barrier Height**	**Transition States**	**Barrier Height**
TS4	33.93	TS4/	54.85

The barrier height for TS4 and TS4/ are 33.93 kcal/mol and 54.85 kcal/mol, respectively. The higher barrier height in both the dimer is due to the fact that O_2 is very slightly activated in IM8 and IM8/. Bond parameters of O_2 in IM8 confirms the inactivated state of O_2 (d_{O-O}=1.245 Å; υ_{O-O}=1371.04 cm^{-1}). Same is the case in IM8/ where bond parameters of O_2 are d_{O-O}=1.235 Å and υ_{O-O}=1422.98 cm^{-1}. Additionally, the considerable distance between two NO molecules makes it challenging for O_2 to react with both of them simultaneously. From Table 4.10, it is evident that $[Au\text{-}Pt]^-$ dimer has a larger activation energy for TER mechanism. This may be attributed to the fact that O_2 is more activated in IM8 than that of IM8/.

4.3.4.3 Termolecular Langmuir Hinshelwood (TLH) mechanism

Another three-molecule reaction process is the termolecular Langmuir Hinshelwood (TLH) [71] mechanism, in which two NO molecules and one O_2 molecule co-adsorb onto the catalyst to interact with one another. Both the dimers have been observed to follow the TLH mechanism. The proposed mechanism for TLH is likely to be followed as (* means attached to the catalyst):

$[Au\text{-}M]^- + 2\ NO\ (gas) + O_2\ (gas) \rightarrow [Au\text{-}M]^-ON^*N^*O\ (coads) + O_2\ (gas)$

$[Au\text{-}M]^-ON^*N^*O\ (coads) + O_2\ (gas) \rightarrow [Au\text{-}M]^-ON^*O^*ON^*O\ (coads)$

$[Au\text{-}M]^-ON^*O^*ON^*O\ (coads) \rightarrow [Au\text{-}M]^-\ O_2N^*N^*O_2\ (coads)$

$[Au\text{-}M]^-\ O_2N^*N^*O_2\ (coads) \rightarrow [Au\text{-}M]^- + 2\ NO_2\ (gas)$

Figure 4.11 and Figure 4.12 demonstrate the optimized geometries of intermediates and transition states involved in the catalytic oxidation pathway of NO on $[Au\text{-}Pd]^-$and $[Au\text{-}Pt]^-$ via TLH mechanism, respectively. Figure 4.13 depicts potential energy diagram for catalytic oxidation pathway of NO on $[Au\text{-}M]^-$ (M=Pd, Pt) dimer via TLH mechanism at M06L/def2TZVP level.

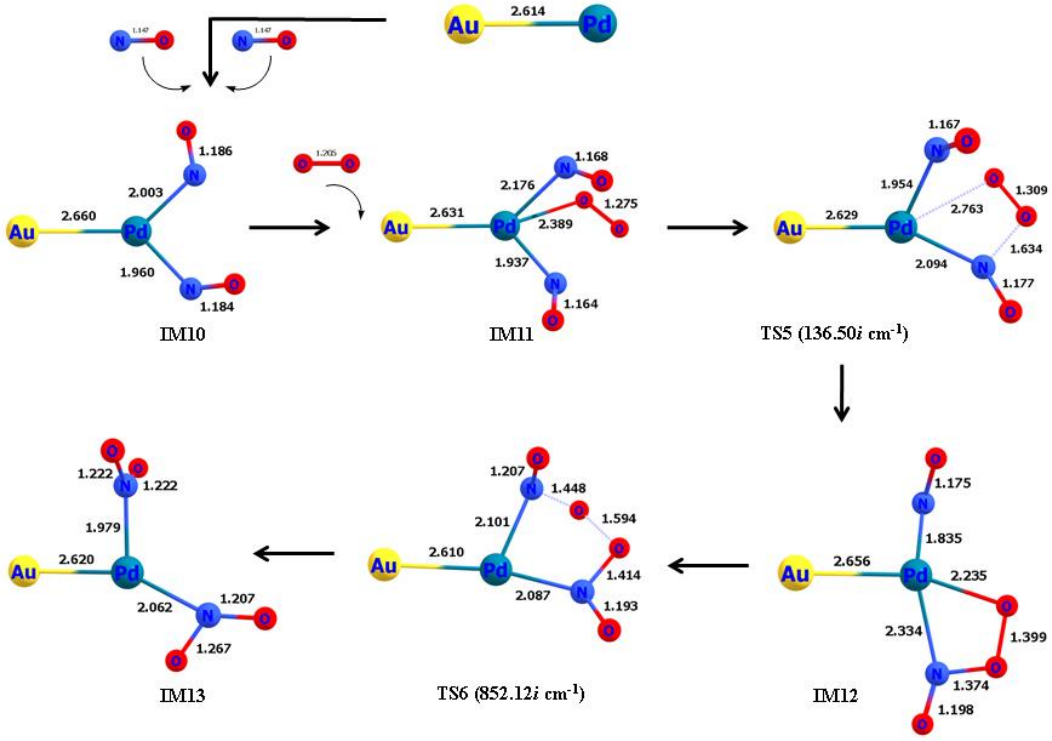

Figure 4.11: Optimized geometries of intermediates and transition states involved in catalytic oxidation pathway of NO on $[Au\text{-}Pd]^-$ dimer via TLH mechanism along with their bond lengths (in Å).

The co-adsorption of two NO molecules onto the Pd atom of $[Au\text{-}Pd]^-$ initiates the process, resulting in the formation of IM10. The activation of both NO molecules in IM10 is demonstrated by their respective bond lengths (1.184 Å and 1.186 Å). This intermediate is 59.07 kcal/mol more stable than the starting point in terms of energy. The addition of one O_2 molecule results in the formation of IM11, an energy intermediate that is more stable (-61.55 kcal/mol in PES). The O_2 molecule is sufficiently active to progress the process, as seen in IM11. The same is reflected in the bond lengths of O_2 (1.275 Å) and $\upsilon_{O\text{-}O}$ (1223.95 cm^{-1}) in IM11. The O atom of O_2 combines with one of the N atoms of NO molecules at TS5 (imaginary frequency=136.50***i*** cm^{-1}) to generate IM12. The activation barrier in this step is 3.27 kcal/mol, and it is exothermic by 6.90 kcal/mol. Therefore, this step is feasible from a thermodynamic and kinetic perspective. The second O atom of O_2 combines with the other NO molecule in the second TS to form a cyclic O-N-O-O-N-O species. This step has an activation barrier of 29.14 kcal/mol and is 45.40 kcal/mol highly exothermic. IM13 is formed way below the starting point (-113.85 kcal/mol),

indicating the high stability of the intermediate. Both of the NO_2 molecules have a desorption energy of 80.72 kcal/mol (40.36 kcal/mol for each NO_2).

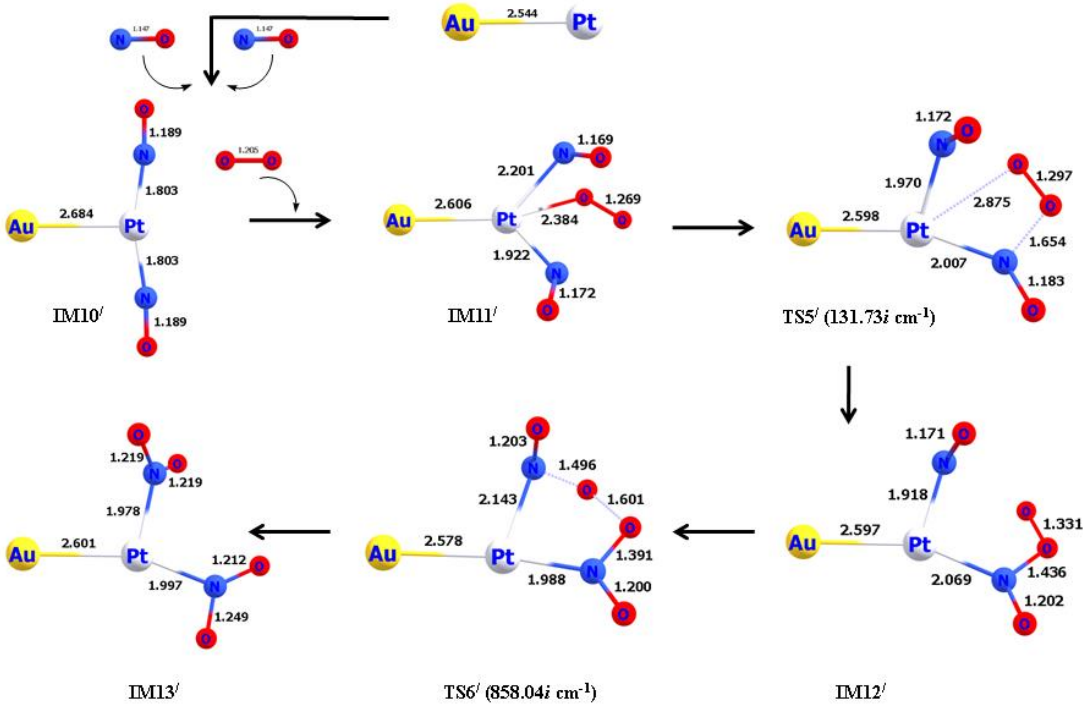

Figure 4.12: Optimized geometries of intermediates and transition states involved in catalytic oxidation pathway of NO on $[Au\text{-}Pt]^-$ dimer via TLH mechanism along with their bond lengths (in Å).

A similar process is also followed on $[Au\text{-}Pt]^-$ dimer. The formation of IM10/ is initiated by the co-adsorption of two NO molecules on the Pt atom of $[Au\text{-}Pt]^-$ dimer. The activation of both NO molecules in IM10/ is evidenced by their respective bond lengths (1.189 Å) and vibrational frequency (1764.99 cm^{-1}). This intermediate has 86.67 kcal/mol higher stability than the reactants in terms of energy. The addition of one O_2 molecule promotes the generation of IM11/. However, IM11/ is a less stable intermediate (-69.03 kcal/mol in PES) with respect to IM10/. Similar to IM11, the O_2 molecule is sufficiently active in IM11/ to move the process along. This is mirrored in the bond lengths of O_2 (1.269 Å) and υ_{O-O} (1245.64 cm^{-1}) in IM11. At TS5 (imaginary frequency=131.73***i*** cm^{-1}), the O atom of O_2 bonds with one of the N atoms of NO molecules to form IM12/ with an activation barrier of 3.55 kcal/mol. This step is slightly endothermic by 2.44 kcal/mol. The second O atom of O_2 reacts with the other NO molecule in the second TS to generate the cyclic O-N-O-O-N-O species. TS6/ has a 21.25 kcal/mol activation barrier and is highly exothermic

(56.19 kcal/mol). At last, IM13/ is produced which is significantly below the starting point (-122.78 kcal/mol), demonstrating the intermediate's excellent stability in PES. Both NO_2 molecules have a desorption energy of 89.65 kcal/mol (44.82 kcal/mol for each NO). It is important to note that the spin is conserved throughout the whole reaction pathway for all the mechanisms previously discussed.

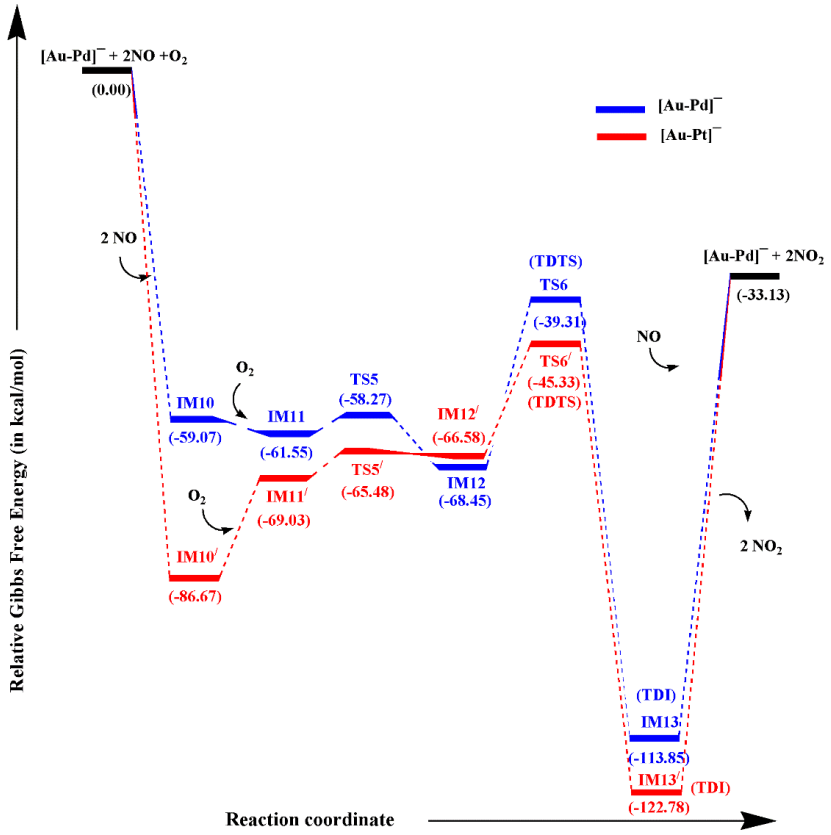

Figure 4.13: Potential energy diagram for catalytic oxidation pathway of NO on $[Au-M]^-$ (M=Pd, Pt) dimer via TLH mechanism at M06L/def2TZVP level. The rate-determining states have been labeled.

Table 4.11: Calculated barrier heights (in kcal/mol) for both the anionic dimers via TLH mechanism at M06L/def2TZVP level.

$[Au-Pd]^-$		**$[Au-Pt]^-$**	
Transition States	**Barrier Height**	**Transition States**	**Barrier Height**
TS5	3.27	TS5/	3.55
TS6	29.14	TS6/	21.25

4.3.4.4 Efficiency of clusters using energetic span model

The energetic span model has been a simple method to analyze the efficiency of a catalyst from a theoretically obtained free energy reaction pathway [72, 73]. It is noteworthy to observe the rate-determining states of the overall reaction mechanism as it suggests where the reaction can be controlled. To find out the efficiency of the two catalytic reactions, we have studied the energetic span model and calculated the value of the energetic span (δE) and TOF using the Eq. 4 and Eq. 3, respectively and provided in Table 4.12. For L-H mechanism, Table 4.12 shows that IM6 correspond to TS2 have a maximum value of 25.23 kcal/mol for NO catalytic oxidation reaction on [Au-Pd]$^-$catalyst. In the case of [Au-Pt]$^-$catalyst, IM5/ correspond to TS3/ has the maximum δE value of 42.96 kcal/mol for L-H mechanism. For TER, IM7 correspond to TS4 has the maximum δE value of 44.66 kcal/mol for [Au-Pd]$^-$catalyst while IM8/ correspond to TS4/ has the maximum δE value of 54.86 kcal/mol for [Au-Pt]$^-$. The maximum δE value for [Au-Pd]$^-$catalyst in TLH mechanism is 41.42 kcal/mol for IM13, which corresponds to TS6, and 44.33 kcal/mol for IM13/, which corresponds to TS6/, for [Au-Pt]$^-$. It is obvious from the calculation that [Au-Pd]$^-$ have a higher turnover frequency and hence, expected to be more efficient via L-H mechanism. The intermediate IM6 (TDI) and the transition state TS2 (TDTS) are found to be rate determining states (RDS) for the more efficient pathway (L-H mechanism).

Table 4.12: Values of key state energies (in kcal/mol), δE value (in kcal/mol) and TOF (in s^{-1}) for [Au-M]$^-$ (M=Pd, Pt) dimers.

Pathways	[Au-Pd]$^-$				[Au-Pt]$^-$			
	TDTS	TDI	δ_E	TOF	TDTS	TDI	δ_E	TOF
L-H	-25.57(TS2)	-83.92(IM6)	25.23	1.90×10^{-6}	-62.17(TS3/)	-105.13(IM5/)	42.96	1.86×10^{-19}
TER	-24.38(TS4)	-69.04(IM7)	44.66	1.05×10^{-20}	-30.99(TS4/)	-85.85(IM8/)	54.86	3.44×10^{-28}
TLH	-39.31(TS6)	-113.85(IM13)	41.42	2.50×10^{-18}	-45.33(TS6/)	-122.78(IM13/)	44.33	1.83×10^{-20}

4.3.4.5 Kinetic analysis

In coal-fired power plants, the temperature of the fuel gas varies between 298.15 K and 1000 K [70]. Here, the Langmuir-Hinshelwood mechanism, which is the most prominent path on the [Au-Pd]$^-$ dimer, has its kinetics examined in the temperature range mentioned above. It is significant to observe that the NO oxidation reaction energy increase as the reaction temperature rises, indicating that an increase in temperature inhibits the spontaneous nature of the reaction. For the L-H mechanism, rate coefficients (in s^{-1}) are shown in Table 4.13 for the temperature range of 298.15–1000 K.

Table 4.13: Calculated rate coefficients (in s^{-1}) within the temperature range of 298.15–1000 K for the L-H mechanism on [Au-Pd]$^-$ at the M06L/def2TZVP level of theory.

Temp (in K)	k_1	k_2	k_3
298.15	2.09×10^{-3}	1.35×10^{6}	2.50×10^{-5}
400	7.89×10^{0}	8.54×10^{7}	6.22×10^{-1}
500	9.75×10^{2}	9.81×10^{8}	2.39×10^{2}
600	2.42×10^{4}	5.03×10^{9}	1.28×10^{4}
700	2.41×10^{5}	1.62×10^{10}	2.20×10^{5}
800	1.35×10^{6}	3.92×10^{10}	1.87×10^{6}
900	5.16×10^{6}	7.78×10^{10}	9.88×10^{6}
1000	1.51×10^{7}	1.35×10^{11}	3.75×10^{7}

Figure 4.14 shows how the logarithm of reaction rate constants varies for the same mechanism at different reaction temperatures. Table 4.13 and Figure 4.14 illustrates clearly that the rate constants always rise as the temperature rises, suggesting that high temperatures might accelerate the catalytic oxidation of NO. Moreover, value of k_2 increases much more with increase in temperature with respect to k_1 and k_3. It suggests that second step of the L-H mechanism on [Au-Pd]$^-$ dimer is the fastest step. Hence, temperature has a promoting effect on the reaction rate of NO oxidation.

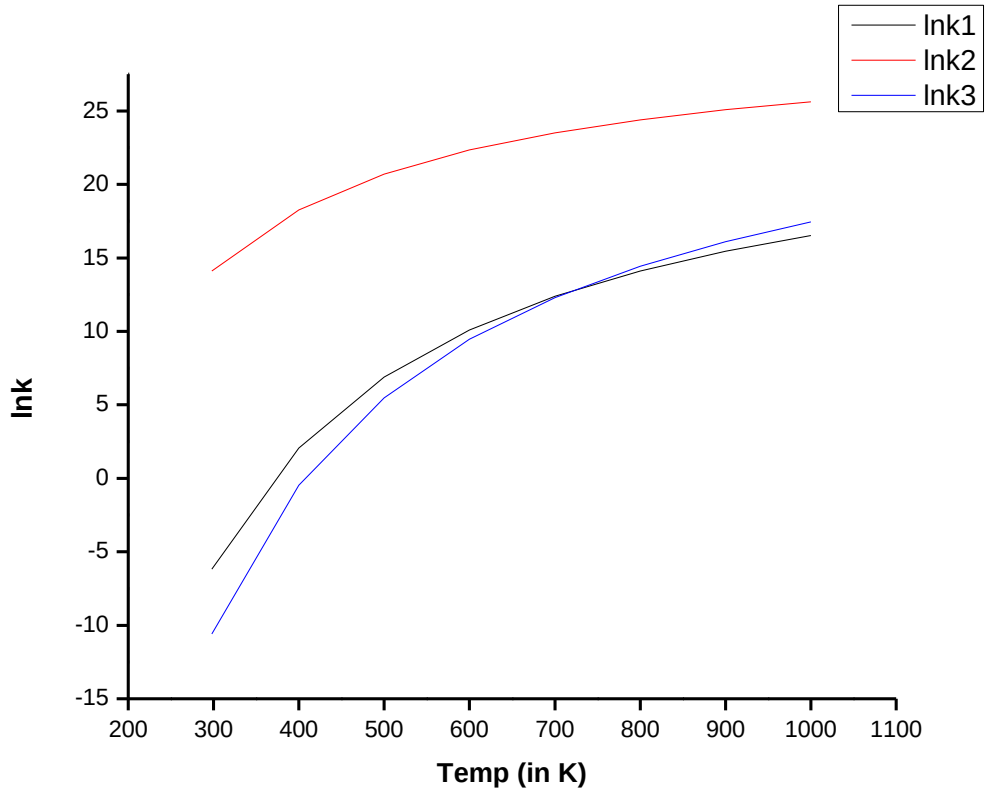

Figure 4.14: Changes in logarithm of reaction rate constants under different reaction temperatures for L-H mechanism.

Moreover, desorption energies of two NO_2 molecules for L-H mechanism at different temperatures has also been studied and tabulated in Table 4.14. It suggests that desorption energies decrease as the temperature rises which means as the temperature increases, it becomes easier for two NO_2 molecules to get desorbed from the catalytic dimer.

Table 4.14: Changes in desorption energies (ΔG_{des}) (in kcal/mol) of two NO_2 molecules for TER-3 mechanism under different reaction temperatures.

Temp	ΔG_{des} (1st NO_2)	ΔG_{des} (2nd NO_2)
298.15	28.47	50.79
400	25.19	47.75
500	22.75	44.84
600	18.39	41.99
700	15.10	39.18
800	11.86	36.42

900	9.68	33.70
1000	6.54	31.01

4.4 Significant Outcomes

In summary, the catalytic oxidation mechanism of NO into NO_2 in the presence of O_2 activated on precious metal dimers, $[Au\text{-}Pd]^-$and $[Au\text{-}Pt]^-$, is investigated.

1. From adsorption energies and NBO calculations, it was established that M sites (M=Pd, Pt) are more preferred for adsorption than the Au site.
2. Co-E_{ads} values also reveal that reactants will co-adsorb at M site of the bimetallic dimer. Hence, reactions were carried out at M sites on both the dimers *via* L-H, TER and TLH mechanisms.
3. Consequently, on comparing the energy barriers and energetic span (δE) for all the three mechanisms, it can be concluded that L-H mechanism is the most preferred pathway for NO oxidation on $[Au\text{-}Pd]^-$dimer.
4. For L-H mechanism, we have observed that there is a difference in the reaction mechanism among the two anionic bimetallic dimers in terms of their calculated reaction energies and activation barriers, particularly in the energy barriers of TS3 (TS3/). The activation barrier for the formation of the second NO_2 (TS3/) is high for $[Au\text{-}Pt]^-$ dimer.
5. The calculation of the energetic span model also concludes the same. IM6 and TS2 are the RDS for $[Au\text{-}Pd]^-$whereas, for $[Au\text{-}Pt]^-$ we have found IM5/ and TS3/ as our RDS. Hence,catalytic NO oxidation goes more smoothly on $[Au\text{-}Pd]^-$ dimer.
6. Finally, our results offer a potential tunability in the catalyst which can act as a future replacement for the reactive metal sites. Along these lines, such modifications also open up a better avenue for experimentalists to explore the oxidation process at atomistic scale for building efficient catalysts in the large scale processes.

4.5 Bibliography

[1] Liu, C., Shi, J. W., Gao, C., and Niu, C. Manganese oxide-based catalysts for low-temperature selective catalytic reduction of NO_x with NH_3: A review. *Applied Catalysis A: General*, 522, 54-69, 2016.

[2] Tang, X., Gao, F., Xiang, Y., Yi, H., Zhao, S., Liu, X., and Li, Y. Effect of potassium-precursor promoters on catalytic oxidation activity of Mn-CoO_x catalysts for NO removal. *Industrial & Engineering Chemistry Research*, 54:9116-9123, 2015.

[3] Zhang, S., Li, H., and Zhong, Q. Promotional effect of F-doped V_2O_5–WO_3/TiO_2 catalyst for NH_3-SCR of NO at low-temperature. *Applied Catalysis A: General*, 435:156-162, 2012.

[4] Li, L., Shen, Q., Cheng, J., and Hao, Z. Catalytic oxidation of NO over TiO_2 supported platinum clusters I. Preparation, characterization and catalytic properties. *Applied Catalysis B: Environmental*, 93:259-266, 2010.

[5] Setiabudi, A., Makkee, M., and Moulijn, J. A. The role of NO_2 and O_2 in the accelerated combustion of soot in diesel exhaust gases. *Applied Catalysis B: Environmental*, 50:185-194, 2004.

[6] Katare, S. R., Patterson, J. E., and Laing, P. M. Diesel aftertreatment modeling: A systems approach to NO_x control. *Industrial & engineering chemistry research*, 46:2445-2454, 2007.

[7] Xue, E., Seshan, K., and Ross, J. R. H. Roles of supports, Pt loading and Pt dispersion in the oxidation of NO to NO_2 and of SO_2 to SO_3. *Applied Catalysis B: Environmental*, 11:65-79, 1996.

[8] Forzatti, P., Castoldi, L., Nova, I., Lietti, L., and Tronconi, E. NO_x removal catalysis under lean conditions. *Catalysis today*, 117:316-320, 2006.

[9] Nova, I., Ciardelli, C., Tronconi, E., Chatterjee, D., and Bandl-Konrad, B. NH_3–NO/NO_2 chemistry over V-based catalysts and its role in the mechanism of the Fast SCR reaction. *Catalysis Today*, 114:3-12, 2006.

[10] Hong, Z., Wang, Z., and Li, X. Catalytic oxidation of nitric oxide (NO) over different catalysts: an overview. *Catalysis Science & Technology*, 7:3440-3452, 2017.

[11] Hernández-Fernández, J., Aguilar-Elguezabal, A., Castillo, S., Ceron-Ceron, B., Arizabalo, R. D., and Moran-Pineda, M. Oxidation of NO in gas phase by Au–TiO_2 photocatalysts prepared by the sol–gel method. *Catalysis Today*, 148:115-118, 2009.

[12] Dawody, J., Skoglundh, M., and Fridell, E. The effect of metal oxide additives (WO_3, MoO_3, V_2O_5, Ga_2O_3) on the oxidation of NO and SO_2 over Pt/Al_2O_3 and

Pt/BaO/Al_2O_3 catalysts. *Journal of Molecular Catalysis A: Chemical*, 209:215-225, 2004.

[13] Zhang, H. L., Zhu, Y., Wang, S. D., Zhao, M., Gong, M. C., and Chen, Y. Q. Activity and thermal stability of Pt/Ce0. 64Mn0. 16R0. 2Ox (R= Al, Zr, La, or Y) for soot and NO oxidation. *Fuel processing technology*, 137:38-47, 2015.

[14] Irfan, M. F., Goo, J. H., Kim, S. D., and Hong, S. C. Effect of CO on NO oxidation over platinum based catalysts for hybrid fast SCR process. *Chemosphere*, 66:54-59, 2007.

[15] Bond, G. C. and Thompson, D. T. Catalysis by gold. *Catalysis Reviews*, 41:319-388, 1999.

[16] Haruta, M. When gold is not noble: catalysis by nanoparticles. *The chemical record*, 3:75-87, 2003.

[17] Valden, M., Lai, X., and Goodman, D. Onset of catalytic activity of gold clusters on titania with the appearance of nonmetallic properties. *science*, 281:1647-1650, 1998.

[18] Daniel, M. C. and Astruc, D. Gold nanoparticles: assembly, supramolecular chemistry, quantum-size-related properties, and applications toward biology, catalysis, and nanotechnology. *Chemical reviews*, 104:293-346, 2004.

[19] Xu, C., Su, J., Xu, X., Liu, P., Zhao, H., Tian, F., and Ding, Y. Low temperature CO oxidation over unsupported nanoporous gold. *Journal of the American Chemical Society*, 129:42-43, 2007.

[20] Socaciu, L. D., Hagen, J., Bernhardt, T. M., Wöste, L., Heiz, U., Häkkinen, H., and Landman, U. Catalytic CO oxidation by free Au_2^-: experiment and theory. *Journal of the American Chemical Society*, 125:10437-10445, 2003.

[21] Fu, Q., Saltsburg, H., and Flytzani-Stephanopoulos, M. Active nonmetallic Au and Pt species on ceria-based water-gas shift catalysts. *Science*, 301:935-938, 2003.

[22] Sakurai, H., Akita, T., Tsubota, S., Kiuchi, M., and Haruta, M. Low-temperature activity of Au/CeO_2 for water gas shift reaction, and characterization by ADF-STEM, temperature-programmed reaction, and pulse reaction. *Applied Catalysis A: General*, 291:179-187, 2005.

[23] Taylor, B., Lauterbach, J., Blau, G. E., and Delgass, W. N. Reaction kinetic analysis of the gas-phase epoxidation of propylene over Au/TS-1. *Journal of catalysis*, 242:142-152, 2006.

[24] Taylor, B., Lauterbach, J., and Delgass, W. N. Gas-phase epoxidation of propylene over small gold ensembles on TS-1. *Applied Catalysis A: General*, 291:188-198, 2005.

[25] Landon, P., Collier, P. J., Carley, A. F., Chadwick, D., Papworth, A. J., Burrows, A., Kiely, C. J., and Hutchings, G. J. Direct synthesis of hydrogen peroxide from H_2 and O_2 using Pd and Au catalysts. *Physical Chemistry Chemical Physics*, 5:1917-1923, 2003.

[26] Chilukuri, S., Joseph, T., Malwadkar, S., Damle, C., Halligudi, S.B., Rao, B.S., Sastry, M. and Ratnasamy, P. Au and Au-Pt bimetallic nanoparticles in MCM-41 materials: applications in co preferential oxidation. *In Studies in Surface Science and Catalysis*, 146:573-576, 2003.

[27] Lou, Y., Maye, M. M., Han, L., Luo, J., and Zhong, C. J. Gold–platinum alloy nanoparticle assembly as catalyst for methanol electrooxidation. *Chemical Communications*, 5:473-474, 2001.

[28] Peng, S. L., Gan, L. Y., Tian, R. Y., and Zhao, Y. J. Theoretical study of CO adsorption and oxidation on the gold–palladium bimetal clusters. *Computational and Theoretical Chemistry*, 977:62-68, 2011.

[29] Zhang, J., Jin, H., Sullivan, M. B., Lim, F. C. H., and Wu, P. Study of Pd–Au bimetallic catalysts for CO oxidation reaction by DFT calculations. *Physical Chemistry Chemical Physics*, 11:1441-1446, 2009.

[30] Enache, D. I., Edwards, J. K., Landon, P., Solsona-Espriu, B., Carley, A. F., Herzing, A. A., Watanabe, M., Kiely, C. J., Knight, D. W., and Hutchings, G. J. Solvent-free oxidation of primary alcohols to aldehydes using Au-Pd/TiO_2 catalysts. *Science*, 311:362-365, 2006.

[31] Jelic, J. and Meyer, R. J. A DFT study of pseudomorphic monolayer Pt and Pd catalysts for NOx storage reduction applications. *Catalysis today*, 136:76-83, 2008.

[32] Olsson, L. and Fridell, E. The influence of Pt oxide formation and Pt dispersion on the reactions $NO_2 \Leftrightarrow NO + 1/2\ O_2$ over Pt/Al_2O_3 and Pt/BaO/Al_2O_3. *Journal of Catalysis*, 210:340-353, 2002.

[33] Despres, J., Elsener, M., Koebel, M., Kröcher, O., Schnyder, B., and Wokaun, A. Catalytic oxidation of nitrogen monoxide over Pt/SiO_2. *Applied Catalysis B: Environmental*, 50:73-82, 2004.

[34] Mulla, S. S., Chen, N., Cumaranatunge, L., Blau, G. E., Zemlyanov, D. Y., Delgass, W. N., Epling, W. S., and Ribeiro, F. H. Reaction of NO and O_2 to NO_2 on Pt: Kinetics and catalyst deactivation. *Journal of Catalysis*, 241:389-399, 2006.

[35] Denton, P., Giroir-Fendler, A., Praliaud, H., and Primet, M. Role of the Nature of the Support (Alumina or Silica), of the Support Porosity, and of the Pt Dispersion in the Selective Reduction of NO by C_3H_6 under Lean-Burn Conditions. *Journal of Catalysis*, 189:410-420, 2000.

[36] Vajda, S., Pellin, M. J., Greeley, J. P., Marshall, C. L., Curtiss, L. A., Ballentine, G. A., Elam, J. W., Catillon-Mucherie, S., Redfern, P. C., Mehmood, F., and Zapol, P. Subnanometre platinum clusters as highly active and selective catalysts for the oxidative dehydrogenation of propane. *Nature materials*, 8:213-216, 2009.

[37] Tyo, E. C. and Vajda, S. Catalysis by clusters with precise numbers of atoms. *Nature nanotechnology*, 10:577-588, 2015.

[38] He, H. and Jagvaral, Y. Electrochemical reduction of CO_2 on graphene supported transition metals–towards single atom catalysts. *Physical Chemistry Chemical Physics*, 19:11436-11446, 2017.

[39] He, H., Morrissey, C., Curtiss, L. A., and Zapol, P. Graphene-supported monometallic and bimetallic dimers for electrochemical CO_2 reduction. *The Journal of Physical Chemistry C*, 122:28629-28636, 2018.

[40] Begum, P. and Deka, R. C. A comparative DFT study on the catalytic oxidation of nitric oxide by Pd_2 and PdM (M= Cu, Rh, Ag, Au, Pt). *Catalysis Letters*, 147:581-591, 2017.

[41] Bhattacharjee, D., Mishra, B. K., Chakrabartty, A. K., and Deka, R. C. Catalytic activity of anionic Au–Ag dimer for nitric oxide oxidation: a DFT study. *New Journal of Chemistry*, 39:2209-2216, 2015.

[42] Deka, R. C., Bhattacharjee, D., Chakrabartty, A. K., and Mishra, B. K. 2014. Catalytic oxidation of NO by Au_2^- dimers: a DFT study. *RSC advances*, 4:5399-5404, 2014.

[43] Liu, P., Song, K., Zhang, D. and Liu, C. A comparative theoretical study of the catalytic activities of Au_2^- and $AuAg^-$ dimers for CO oxidation. *Journal of molecular modeling*, 18:1809-1818, 2012.

[44] Gao, Y., Shao, N., Pei, Y., Chen, Z., and Zeng X. C. Catalytic activities of subnanometer gold clusters (Au_{16}–Au_{18}, Au_{20}, and Au_{27}–Au_{35}) for CO oxidation. *ACS nano*, 5:7818-7829, 2011.

[45] Kozuch, S. and Shaik, S. How to conceptualize catalytic cycles? The energetic span model. *Accounts of chemical research*, 44:101-110, 2011.

[46] Frisch, M. J., Trucks, G. W., Schlegel, H. B., Scuseria, G. E., Robb, M. A., Cheeseman, J. R., Scalmani, G., Barone, V., Mennucci, B., Petersson, G. A., Nakatsuji, H., Li, X., Caricato, M., Marenich, A. V., Bloino, J., Janesko, B. G., Gomperts, R., Mennucci, B., Hratchian, H. P., Ortiz, J. V., Izmaylov, A. F., Sonnenberg, J. L., Williams-Young, D., Ding, F., Lipparini, F., Egidi, F., Goings, J., Peng, B., Petrone, A., Henderson, T., Ranasinghe, D., Zakrzewski, V. G., Gao, J., Rega, N., Zheng, G., Liang, W., Hada, M., Ehara, M., Toyota, K., Fukuda, R., Hasegawa, J., Ishida, M., Nakajima, T., Honda, Y., Kitao, O., Nakai, H., Vreven, T., Throssell, K., Montgomery, J. A. Jr., Peralta, J. E., Ogliaro, F., Bearpark, M. J., Heyd, J. J., Brothers, E. N., Kudin, K. N., Staroverov, V. N., Keith, T. A., Kobayashi, R., Normand, J., Raghavachari, K., Rendell, A. P., Burant, J. C., Iyengar, S. S., Tomasi, J., Cossi, M., Millam, J. M., Klene, M., Adamo, C., Cammi, R., Ochterski, J. W., Martin, R. L., Morokuma, K., Farkas, O., Foresman, J. B., Fox, D. J. Gaussian 09, Revision D. 01, Gaussian, Inc., Wallingford CT, 2009.

[47] Zhao, Y. and Truhlar, D. G. A new local density functional for main-group thermochemistry, transition metal bonding, thermochemical kinetics, and noncovalent interactions. *The Journal of chemical physics*, 125(19), 194101, 2006.

[48] Boekfa, B., Pahl, E., Gaston, N., Sakurai, H., Limtrakul, J., and Ehara, M. C–Cl bond activation on Au/Pd bimetallic nanocatalysts studied by density functional theory and genetic algorithm calculations. *The Journal of Physical Chemistry C*, 118:22188-22196, 2014.

[49] Boekfa, B., Treesukol, P., Injongkol, Y., Maihom, T., Maitarad, P., and Limtrakul, J. The activation of methane on Ru, Rh, and Pd decorated carbon nanotube and boron nitride nanotube: a DFT study. *Catalysts*, 8:190, 2018.

[50] Maitarad, P., Namuangruk, S., Zhang, D., Shi, L., Li, H., Huang, L., Boekfa, B., and Ehara, M. Metal–porphyrin: a potential catalyst for direct decomposition of N_2O by theoretical reaction mechanism investigation. *Environmental science & technology*, 48:7101-7110, 2014.

[51] Vilhelmsen, L. B. and Hammer, B. Systematic Study of Au_6 to Au_{12} Gold Clusters on MgO (100) F Centers Using Density-Functional Theory. *Physical review letters*, 108:126101, 2012.

[52] Ferrighi, L., Hammer, B., and Madsen, G. K. 2D− 3D transition for cationic and anionic gold clusters: a kinetic energy density functional study. *Journal of the American Chemical Society*, 131:10605-10609, 2009.

[53] Weigend, F. and Ahlrichs, R. Balanced basis sets of split valence, triple zeta valence and quadruple zeta valence quality for H to Rn: Design and assessment of accuracy. *Physical Chemistry Chemical Physics*, 7:3297-3305, 2005.

[54] Weigend, F. Accurate Coulomb-fitting basis sets for H to Rn. *Physical chemistry chemical physics*, 8:1057-1065, 2006.

[55] Gonzalez, C. and Schlegel, H. B. Improved algorithms for reaction path following: higher-order implicit algorithms. *The Journal of chemical physics*, 95:5853-5860, 1991.

[56] Pople, J. A., Head-Gordon, M., and Raghavachari, K. Quadratic configuration interaction. A general technique for determining electron correlation energies. *The Journal of chemical physics*, 87:5968-5975, 1987.

[57] Foster, J. P. and Weinhold, F. Natural hybrid orbitals. *Journal of the American Chemical Society*, 102:7211-7218, 1980.

[58] IMAll (Version 17.01.25), Todd A. Keith, TK Gristmill Software, Overland Park KS,USA, 2017. <aim.tkgristmill.com>

[59] Kozuch, S. A refinement of everyday thinking: the energetic span model for kinetic assessment of catalytic cycles. *Wiley Interdisciplinary Reviews: Computational Molecular Science*, 2:795-815, 2012.

[60] Kozuch, S. and Martin, J. M. What makes for a bad catalytic cycle? A theoretical study on the Suzuki− Miyaura reaction within the energetic span model. *ACS Catalysis*, 1:246-253, 2011.

[61] Laidler, K. J. *Chemical Kinetics*, Pearson Education, 3rd edition, 2008.

[62] Lide D. R. *CRC handbook of chemistry and physics*, CRC Press, New York, 89th edition, 2009.

[63] Chen, X., Lu, R. F., Kan, E. J., Liu, Y. Z., Xiao, C. Y., and Deng, K. M. Theoretical study of CO oxidation on cationic, neutral, and anionic AuM dimers (M= Pd and Ag). *Journal of molecular modeling*, 20:1-10, 2014.

[64] Posada-Borbón, A. and Posada-Amarillas, A. Theoretical DFT study of homonuclear and binary transition-metal dimers. *Chemical Physics Letters*, 618:66-71, 2015.

[65] Wiberg, K. B. Application of the pople-santry-segal CNDO method to the cyclopropylcarbinyl and cyclobutyl cation and to bicyclobutane.*Tetrahedron,* 24:1083-1096, 1968.

[66] Torres, D., González, S., Neyman, K. M., and Illas, F. Adsorption and oxidation of NO on Au (1 1 1) surface: Density functional studies. *Chemical physics letters*, 422:412-416, 2006.

[67] Olsson, L., Persson, H., Fridell, E., Skoglundh, M., and Andersson, B. A kinetic study of NO oxidation and NO_x storage on Pt/Al_2O_3 and $Pt/BaO/Al_2O_3$. *The Journal of Physical Chemistry B*, 105:6895-6906, 2001.

[68] Tang, Y., Chen, W., Zhao, G., Teng, D., Cui, Y., Li, Z., Feng, Z., and Dai, X. Comparative Study of NO and CO Oxidation Reactions on Single-Atom Catalysts Anchored Graphene-like Monolayer. *ChemPhysChem*, 22:606-618, 2021.

[69] Tang, Y., Zhou, J., Chen, W., Chai, H., Li, Y., Feng, Z., and Dai, X. Theoretical evaluation on single-atom Fe doped divacancy graphene for catalytic CO and NO oxidation by O_2 molecules. *Molecular Catalysis*, 476:110524, 2019.

[70] Yang, W., Gao, Z., Liu, X., Li, X., Ding, X., and Yan, W. Single-atom iron catalyst with single-vacancy graphene-based substrate as a novel catalyst for NO oxidation: a theoretical study. *Catalysis Science & Technology*, 8:4159-4168, 2018.

[71] Zhu, C., Liang, J.X., Wang, Y.G. and Li, J. Non-noble metal single-atom catalyst with MXene support: Fe_1/Ti_2CO_2 for CO oxidation. *Chinese Journal of Catalysis*, 43:1830-1841, 2022.

[72] Jindal, G. and Sunoj, R. B. Importance of ligand exchanges in Pd (II)-Brønsted acid cooperative catalytic approach to spirocyclic rings. *Journal of the American Chemical Society*, 136:15998-16008, 2014.

[73] Das, D., Jain, P., Pal, S., and Avasare, V. Mechanistic Investigations of Aluminum Nitrite Assisted Aryl Nitrile Synthesis through C (sp^3)–C (sp^2) Bond Cleavage of Aryl Ketones. *The Journal of Physical Chemistry C*, 123:2343